Monthly Notices
of the
ROYAL ASTRONOMICAL SOCIETY

MNRAS **471,** 4005–4026 (2017)
Advance Access publication 2017 July 20

doi:10.1093/mnras/stx1835

Integral-field kinematics and stellar populations of early-type galaxies out to three half-light radii

Nicholas Fraser Boardman,[1⋆] Anne-Marie Weijmans,[1] Remco van den Bosch,[2] Harald Kuntschner,[3] Eric Emsellem,[3,4] Michele Cappellari,[5] Tim de Zeeuw,[3,6] Jesus Falcón-Barroso,[7,8] Davor Krajnović,[9] Richard McDermid,[10,11] Thorsten Naab,[12] Glenn van de Ven[2] and Akin Yildirim[2]

[1]*School of Physics and Astronomy, University of St Andrews, North Haugh, St Andrews KY16 9SS, UK*
[2]*Max Planck Institute for Astronomy, Königstuhl 17, D-69117 Heidelberg, Germany*
[3]*European Southern Observatory, Karl-Schwarzschild-Str. 2, D-85748 Garching, Germany*
[4]*Université Lyon 1, Observatoire de Lyon, Centre de Recherche Astrophysique de Lyon and Ecole Normale Supérieure de Lyon, 9 avenue Charles André, F-69230 Saint-Genis Laval, France*
[5]*Sub-department of Astrophysics, Department of Physics, University of Oxford, Denys Wilkinson Building, Keble Road, Oxford OX1 3RH, UK*
[6]*Sterrewacht Leiden, Leiden University, Postbus 9513, NL-2300 RA Leiden, the Netherlands*
[7]*Instituto de Astrofisica de Canarias, E-38200, La Laguna, Spain*
[8]*Depto. Astrofisica, Universidad de La Laguna (ULL), E-38206 La Laguna, Tenerife, Spain*
[9]*Leibniz-Institut für Astrophysik Potsdam (AIP), An der Sternwarte 16, D-14482 Potsdam, Germany*
[10]*Department of Physics and Astronomy, Macquarie University, Sydney, NSW 2109, Australia*
[11]*Australian Astronomical Observatory, PO Box 915, North Ryde, NSW 1670, Australia*
[12]*Max-Planck-Institut für Astrophysik, Karl-Schwarzschild-Str. 1, D-85741 Garching, Germany*

Accepted 2017 July 18. Received 2017 July 17; in original form 2017 February 16

ABSTRACT

We observed 12 nearby H I-detected early-type galaxies (ETGs) of stellar mass $\sim 10^{10}\,M_\odot \leq M_* \leq \sim 10^{11}\,M_\odot$ with the Mitchell Integral-Field Spectrograph, reaching approximately three half-light radii in most cases. We extracted line-of-sight velocity distributions for the stellar and gaseous components. We find little evidence of transitions in the stellar kinematics of the galaxies in our sample beyond the central effective radius, with centrally fast-rotating galaxies remaining fast-rotating and centrally slow-rotating galaxies likewise remaining slow-rotating. This is consistent with these galaxies having not experienced late dry major mergers; however, several of our objects have ionized gas that is misaligned with respect to their stars, suggesting some kind of past interaction. We extract Lick index measurements of the commonly used H β, Fe5015, Mg b, Fe5270 and Fe5335 absorption features, and we find most galaxies to have flat H β gradients and negative Mg b gradients. We measure gradients of age, metallicity and abundance ratio for our galaxies using spectral fitting, and for the majority of our galaxies find negative age and metallicity gradients. We also find the stellar mass-to-light ratios to decrease with radius for most of the galaxies in our sample. Our results are consistent with a view in which intermediate-mass ETGs experience mostly quiet evolutionary histories, but in which many have experienced some kind of gaseous interaction in recent times.

Key words: ISM: kinematics and dynamics – galaxies: elliptical and lenticular, cD – galaxies: evolution – galaxies: ISM – galaxies: kinematics and dynamics – galaxies: structure.

1 INTRODUCTION

The evolutionary paths of lenticular (S0) and elliptical (E) galaxies, collectively referred to as early-type galaxies (ETGs), continue to be of great interest, with ETGs commonly thought to represent the endpoints of galaxy evolution. ETG imaging has repeatedly shown a dramatic size evolution since redshift $z \simeq 2$, with massive ETGs (those with stellar masses $M_* \geq \sim 10^{11}\,M_\odot$) significantly smaller and more compact in the past than in the present day (Trujillo et al. 2006; van Dokkum et al. 2010, 2013; Cimatti, Nipoti & Cassata 2012). This size evolution can be explained by a

⋆ E-mail: nfb@st-andrews.ac.uk

'two-phase' picture of ETG formation (Oser et al. 2010, 2012). In this picture, a dense core is formed at early times ($z \simeq 2$) via strongly dissipative processes. Star formation is quenched subsequently, and then a stellar halo is built up over time from dry merging and accretion episodes.

Further information on ETGs may be obtained from spectroscopic observations. In particular, two-dimensional spectroscopy from the SAURON instrument (Bacon et al. 2001) by the SAURON (de Zeeuw et al. 2002) and ATLAS^{3D} (Cappellari et al. 2011a) surveys have greatly enhanced our understanding of ETGs' structures. ETGs can be slow rotating or fast rotating, with a wide range of kinematic substructures reported in individual systems (Krajnović et al. 2011); as such, ETGs may be classed as 'fast rotators' (FRs) or 'slow rotators' (SRs), based on their line-of-sight kinematics (Emsellem et al. 2007, 2011). More massive ETGs are also more likely to be SRs, while less massive ones are more likely to be FRs (Emsellem et al. 2011).

A key finding is that FRs, which dominate the ETGs population below a characteristic galaxy stellar mass $M_{\rm crit} \simeq 2 \times 10^{11}$ M$_\odot$, have a velocity dispersion σ that correlates well with galaxy properties like colour, age, the stellar initial mass function and the molecular gas fraction (Cappellari et al. 2013a). Given that σ correlates with the galaxy bulge mass fraction, this suggests that the evolution of fast-rotating ETGs is linked closely to central mass growth, slow-rotating ETGs, which dominate at masses above $M_{\rm crit}$, appear to evolve in some other way. The structure of fast-rotator ETGs was also shown to parallel that of spiral galaxies (Cappellari et al. 2011b) and to lie near parallel with respect to spirals on the mass-size plane, with ETGs systematically smaller (i.e. more concentrated) at a given mass (Cappellari et al. 2013b). These findings are consistent with a view in which ETGs form via two main channels: FRs start as star-forming discs and grow their bulges via dissipative processes, followed by quenching, while the more massive SRs form as in the two-phase scenario described above, with an early rapid dissipative formation followed by repeated dry merger events (see Cappellari 2016, for a review.)

The exact nature of the ETG-spiral link remains unclear. Results from the CALIFA integral field unit (IFU) survey have shown that ETGs on average have less angular momentum and are more centrally concentrated than spiral galaxies (Falcón-Barroso, Lyubenova & van de Ven 2015), which is consistent with results from major merger simulations (Querejeta et al. 2015). Querejeta et al. (2015) point out that some spiral galaxies (particularly Sa galaxies) do indeed overlap with ETGs on the momentum-concentration plane, which is consistent with passive fading scenarios (e.g. Dressler et al. 1997; Peng, Maiolino & Cochrane 2015). Such scenarios are also consistent with measurements of total luminosity and disc scalelength, which are larger for Sa galaxies than for S0s galaxies (Vaghmare et al. 2015). At the same time, around half of local ETGs display significant star-gas misalignments both for neutral gas (Serra et al. 2014) and also for ionized gas (e.g. Sarzi et al. 2006; Davis et al. 2011); this implies that some kind of interaction event must have occurred in a large fraction of ETGs.

One way to study ETGs further is to measure their stellar kinematics to $2R_e$ and beyond – something not possible for much of the ATLAS^{3D} and CALIFA data sets – in order to test if the kinematics are consistent with currently proposed formation scenarios. Arnold et al. (2014) present slitlet stellar kinematics for 22 ETGs from the SLUGGS survey (Brodie et al. 2014) out to 2–4R_e and find kinematic transitions in a few of their objects, with abrupt drops in the angular momentum beyond $1R_e$; Arnold et al. (2014) argue this to be evidence of two-phase formation in these objects, with the momentum drops signifying a transition to accretion-dominated stellar haloes. By contrast, Raskutti, Greene & Murphy (2014) do not report finding such transitions from Mitchell Spectrograph IFU observations of their massive ETGs out to 2–5R_e. In addition, galaxies produced in cosmological simulations rarely display such drops in momentum, even for galaxies with significant dry accretion at late times (Naab et al. 2014; Wu et al. 2014).

Further information on ETGs' histories is encoded within the properties of their stellar populations. Most ETGs' stellar light is dominated by old stars, as expected from their 'red and dead' appearance. In addition, compact ETGs are older, more metal rich and more alpha enhanced than more extended ETGs of the same mass; this can be understood as being a result of dissipative galaxy mergers (Cappellari et al. 2013a; McDermid et al. 2015), which drive central galaxy formation and so increase the compactness of a galaxy (Khochfar & Silk 2006). No dependence on size is found for ETGs' stellar population properties at a given velocity dispersion σ, suggesting that σ (and not mass) is the strongest individual indicator of ETGs' stellar populations (Cappellari et al. 2006; Graves, Faber & Schiavon 2009; Cappellari et al. 2013a). At a given dispersion σ, galaxies with a more massive black hole (BH) appear to be older and more alpha enhanced (Martín-Navarro et al. 2016), suggesting that the BH of a galaxy must also play a role; for massive active galaxies in particular, the central BH likely plays a significant part in its host galaxies' quenching (see Fabian 2012, for a review).

Within individual ETGs, various radial gradients have been reported for their stellar population properties in recent years. ETGs have repeatedly been found to have negative metallicity gradients (e.g. Davies, Sadler & Peletier 1993; Rawle et al. 2008; Greene et al. 2013, 2015; Scott et al. 2013; Wilkinson et al. 2015), along with age gradients that are flat or close to flat (e.g. Rawle et al. 2008; Scott et al. 2013; Wilkinson et al. 2015). The metallicity gradients of some ETGs have also been found to change with radius, reflecting their different formation histories. Massive ETGs have been consistently reported to show flattening metallicity gradients beyond $\simeq 1R_e$, consistent with the gradients being 'washed out' by repeated dry accretion events (e.g. Coccato, Gerhard & Arnaboldi 2010; Greene et al. 2013; Pastorello et al. 2014), while less massive ETGs show no such feature (Weijmans et al. 2009; Pastorello et al. 2014). However, only a handful of galaxies significantly below $M_{\rm crit}$ have been studied in this way to date, making it unclear if this picture holds for *all* low-mass ETGs; if low-mass ETGs are linked to spiral galaxies and have evolved via mainly internal processes, then this should indeed be the case.

It is also interesting to consider how the stellar mass-to-light ratio M_*/L varies across a given ETG. M_*/L is typically assumed constant across ETGs for dynamical modelling purposes. However, the above-described stellar population gradients imply that gradients in M_*/L should also be expected. Tortora et al. (2011) fit stellar population models to Sloan Digital Sky Survey (SDSS; Ahn et al. 2014) imaging out to $1R_e$ and find shallow M_*/L drops for ETGs with old centres and shallow rises for ETGs with young centres. Stellar population modelling of spectra out to multiple R_e is a powerful way in which to investigate this point further.

The Mitchell Integral-Field Spectrograph (Hill et al. 2008), on the Harlan J. Smith telescope, is an ideal tool for investigating ETGs' structures beyond $1R_e$. It has a 1.68×1.68 arcmin field of view and uses large individual optical fibres (radius 2.08 arcsec) that are well optimized for deep observations of objects and that reduce the need for spatial binning.

Here, we present results for 12 nearby $\sim 10^{10}$ M$_\odot \leq M_* < M_{\rm crit}$ ETGs observed with the Mitchell Spectrograph. Our observations

Table 1. Summary of our Mitchell Spectrograph sample of ETGs. RA, DEC, R_e, T-type, K-band magnitude M_K and distances are from Cappellari et al. (2011a) and references therein. $\log_{10}(M_*)$ was calculated using the K-band magnitudes, after applying equation (2) in Cappellari (2013). The FR/SR classifications are the $1R_e$ classifications reported in Emsellem et al. (2011).

Galaxy	RA	Dec.	T-type	FR/SR	R_e(arcsec)	M_K	Distance (Mpc)	$\log_{10}(M_*)$
NGC 680	27.447035	21.970827	−4.0	FR	14.5	−24.17	37.5	11.09
NGC 1023	40.100052	39.063251	−2.7	FR	47.9	−24.01	11.1	11.02
NGC 2685	133.894791	58.734409	−1.0	FR	25.7	−22.78	16.7	10.48
NGC 2764	137.072983	21.443447	−2.0	FR	12.3	−23.19	39.6	10.66
NGC 3522	166.668549	20.085621	−4.9	SR	10.2	−21.67	25.5	9.99
NGC 3626	170.015808	18.356791	−1.0	FR	25.7	−23.30	19.5	10.71
NGC 3998	179.484039	55.453564	−2.1	FR	20.0	−23.33	13.7	10.73
NGC 4203	183.770935	33.197243	−2.7	FR	29.5	−23.44	14.7	10.77
NGC 5582	215.179703	39.693584	−4.9	FR	27.5	−23.28	27.7	10.70
NGC 5631	216.638687	56.582664	−1.9	SR	20.9	−23.70	27.0	10.89
NGC 6798	291.013306	53.624752	−2.0	FR	16.9	−23.52	37.5	10.80
UGC 03960	115.094856	23.275089	−4.9	SR	17.4	−21.89	33.2	10.09

reach past $2R_e$ in most cases. We present stellar and gaseous kinematics and absorption line index measurements. We also present results from stellar population modelling. All of our ETGs have previously been observed as part of the ATLAS^{3D} survey, making our own observations greatly complementary.

The structure of this paper is as follows. We discuss our observations and data reduction in Section 2. We describe the extraction of stellar and ionized gas kinematics in Section 3, wherein we also parametrize the stellar angular momentum, of our galaxies as a function of radius. We describe the extraction of absorption line indices in Section 4, and we then explain the calculation of stellar population parameters through spectral fitting in Section 5. We discuss our findings in Section 6 and we conclude in Section 7.

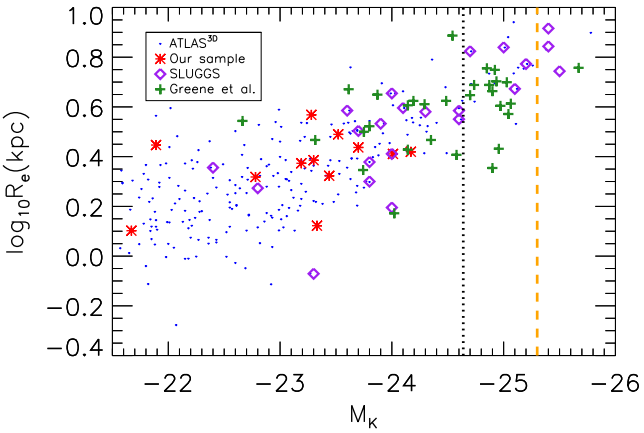

Figure 1. Plot of R_e against absolute K-band magnitude for the full ATLAS^{3D} ETG sample (blue dots), our selected ETGs overlaid (red crosses), the SLUGGS sample (purple diamonds) and the sample of Raskutti et al. (2014) (green pluses). The vertical dotted line corresponds to $M_{\rm crit} = 2 \times 10^{11} M_{\odot}$, using equation (2) from Cappellari (2013), while the orange dashed line corresponds to the upper magnitude limit of the MASSIVE survey (Ma et al. 2014). Our sample focusses on a somewhat lower mass region than SLUGGS, Greene et al. (2013) or MASSIVE.

2 SAMPLE AND DATA REDUCTION

In Table 1, we present our sample of 12 nearby ETGs. We manually selected our sample from the ATLAS^{3D} survey on the basis of detected H I emission from the Westerbork Synthesis Radio Telescope (Serra et al. 2012). NGC 680 and NGC 1023 are both classified as 'u' in Serra et al. (2012), indicating substantially unsettled H I morphology; the remaining 10 sample galaxies contain large-scale regularly rotating H I structures (the 'D' galaxies in Serra et al. 2012). Serra et al. (2014) present H I velocity maps for all H I detected ATLAS^{3D} galaxies, including the galaxies in our sample, so we direct the interested reader to that paper.

In Fig. 1, we compare our sample to those of ATLAS^{3D} and SLUGGS (Arnold et al. 2014), as well as with the massive ETG sample presented in Greene et al. (2013) and Raskutti et al. (2014). We also show the upper magnitude limit of the MASSIVE ETG survey (Ma et al. 2014) on the same figure. We show that the masses of our sample tend towards lower values than the latter three samples, making our sample different from other wide-field samples published thus far. Our sample galaxies all have masses which fall below or around 10^{11} M$_{\odot}$. We obtained M_K and R_e values for our sample from table 3 of Cappellari et al. (2011a), converting the latter to units of kpc using the distances provided in that table; we obtained R_e values for the full ATLAS^{3D} sample in the same manner. We obtained R_e values, distances and M_K quantities for the SLUGGS survey from table 1 of Arnold et al. (2014). We extracted R_e and M_K quantities for the Raskutti et al. (2014) objects directly from their fig. 1.

Observations were taken on the Mitchell spectrograph using the VP2 grating over 27 nights, spaced over four observing runs. Galaxies were observed using a series of 30-min exposures, with bracketing sky observations of 15 min also taken to enable sky subtraction. Bias frames, flat frames and arc frames were taken at the beginning and end of each night, with Ne+Cd comparison lamps used for the arc frames in all cases. We observed some galaxies longer than others, owing to observing time constraints. We also chose to observe certain galaxies over multiple pointings to better capture their structure beyond the central effective radius.

The Mitchell spectrograph has a one-third fill factor, and complete sky coverage can be achieved by taking observations over three dither positions. We observed most galaxies over all three dither positions in order to obtain full coverage. However, a couple

of galaxies could not be observed in this way due to observing time constraints: NGC 4203 was observed over two dither positions instead, while NGC 2685 was also observed over two dither positions over one of its two pointings.

We reduced all data using the custom-built VACCINE pipeline (Adams et al. 2011). VACCINE subtracts science frames of overscan and bias, traces fibres along the charge-coupled device (CCD) chip, calculates wavelength solutions, constructs sky frames using bracketing sky exposures and detects cosmic rays, before collapsing the output science images into a set of one-dimensional spectra. It uses techniques similar to those proposed by Kelson (2003) in order to avoid the resampling of data and, in turn, correlated errors.

We perform sky subtraction at this point by averaging over bracketing sky observations for the purpose of quality control and to estimate the signal-to-noise ratio (S/N) of galaxy spectra. This approach implicitly assumes that the sky varies linearly as a function of time; however, sky variations will actually be non-linear in practice, which can become significant in cases where the sky spectrum dominates the observed light (e.g. Blanc et al. 2013). Therefore, we will later fit the sky spectra as part of the kinematic extraction discussed in Section 3.

We found that some fibres fell off the CCD chip and also found that certain fibres had insufficient wavelength ranges for the bright 5400.56 Å Ne line to be visible; we masked such fibres in our analysis to enable a consistent wavelength range of 4800–5400 Å and to make the derived wavelength solutions as robust as possible. All such fibres were located near the edge of the CCD chip, so removing them has a minimal effect on our analysis.

We combined all science frames into a single spectral data cube for each galaxy, with all spectra for a given galaxy interpolated on to a common linear wavelength scale. We masked out fibre positions with excessively low S/N in all cases. We calculated the instrumental resolutions of the galaxy spectra by fitting Gaussians to the 5154.660 and 5400.56 Å emission lines in the master arc frames, weighting the frames in accordance with that galaxy's observation dates. We found the spectral resolution to vary smoothly as a function of fibre position; we therefore chose to fit a fifth-order polynomial to the resolution as a function of fibre position to eliminate the noise inherent in this calculation. The lowest spectral full width at half-maximum (FWHM) that we found from this process is 1.2 Å with the maximum derived value being 1.7 Å; the latter value corresponds to an instrumental velocity dispersion of approximately 42 km s^{-1}.

In Fig. 2, we compare the radial extent of our data, parametrized via the $R_{\rm max}$ parameter – the maximum aperture radius of the data (e.g. Emsellem et al. 2011) – with that of the ATLAS$^{\rm 3D}$ and SLUGGS samples. We define $R_{\rm max}$ to be the maximum radius of a circular aperture with area equal to an ellipse that is at least 85 per cent filled with spectra; we symmetrized the fibre positions for NGC 1023 and NGC 3626 when calculating $R_{\rm max}$, due to these galaxies not being centred on our field of view (FOV). We find our FOV to be comparable with that of SLUGGS for less massive ETGs, with our data extending beyond $2R_e$ in most cases; our data are therefore highly complementary with respect to the ATLAS$^{\rm 3D}$ data. We obtain ATLAS$^{\rm 3d}$ $R_{\rm max}$ values from table B1 in Emsellem et al. (2011), using the same R_e values as before, and we obtain SLUGGS $R_{\rm max}$ values using table 1 of Arnold et al. (2014).

We found it necessary to bin spectra in galaxies' outer regions in order to improve the S/N. For each galaxy, we broadened all input spectra to the largest measured FWHM for that galaxy and we binned the spectra using the publicly available Voronoi Binning algorithm (Cappellari & Copin 2003). We used a target S/N of 20 per spectral pixel (≃30 per angstrom) for all galaxies. We detail the observation times, observation date, number of pointings and achieved $R_{\rm max}$ for each galaxy in Table 2.

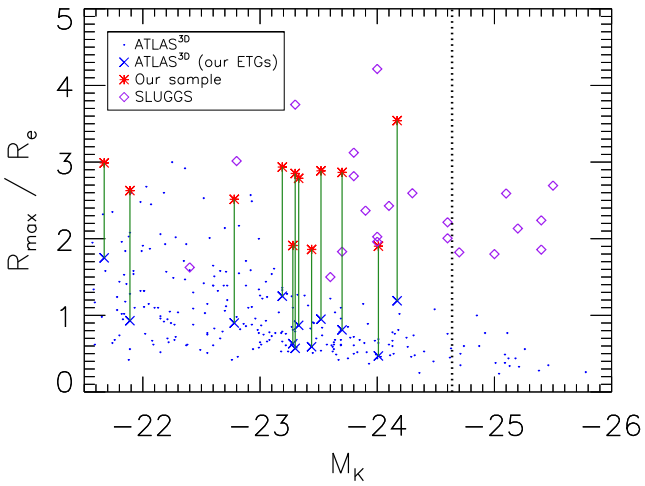

Figure 2. Plot of $R_{\rm max}/R_e$. Blue crosses represent the ATLAS$^{\rm 3D}$ values for our galaxies and green lines show the difference between our values and the ATLAS$^{\rm 3D}$ ones. All other lines and symbols are as before. Our coverage beyond $2R_e$ in many cases and is comparable to the coverage of SLUGGS over lower mass ETGs, whereas ATLAS$^{\rm 3D}$ generally reaches approximately $1R_e$.

2.1 Flux calibration

Due to a lack of suitable flux star observations, we were unable to flux calibrate our Mitchell spectra in the usual way. We therefore performed flux calibration by comparing our spectra for NGC 3522 to the SDSS spectrum for the same system, and then further comparing our galaxy spectra with those of the ATLAS$^{\rm 3D}$ survey. We describe this process in the remainder of this subsection. NGC 3522 is one of two galaxies that we have in common with the Sloan spectral sample, the other being UGC 03960, while all of our galaxies have ATLAS$^{\rm 3D}$ spectra.

As we would be using SDSS data to construct our final flux correction curve, we first verified that the SAURON and SDSS data sets were consistent. We took the SDSS spectrum for NGC 3522 and obtained an equivalent SAURON spectrum by summing over a 3 arcsec aperture in order to match the SDSS fibre radius. We matched the spectral resolutions and then smoothed both spectra. We divided the spectra through and fitted a seventh-order polynomial to derive a correction curve. We find the resulting curve to be almost flat over most of the SAURON wavelength region, as shown in Fig. 3. From this, we conclude that the flux calibration for NGC 3522 is consistent between ATLAS$^{\rm 3D}$ and SDSS.

Next, we considered whether a single flux-calibration curve would be valid for our sample. We compared the central Mitchell spectrum for each galaxy with a SAURON spectrum obtained by summing over an equivalent region, and calculated correction curves in the same manner described above. We show the results of this process in Fig. 4. We find that the flux-calibration curves are broadly similar across the whole sample, and so conclude that a single calibration curve will indeed be valid for our galaxies.

We obtained an initial correction curve by comparing our central Mitchell spectrograph spectrum for NGC 3522 with the corresponding SDSS spectrum, with the calibration curve derived in the same manner as before. We applied this curve to all Mitchell spectra, and we show the resulting Mitchell-to-SAURON curves in the left-hand

Table 2. Summary of Mitchell spectrograph data for our ETGs, in terms of observation time, date of observing run, number of pointings and achieved (circular) aperture radius R_{max}. The kpc values of R_{max} were calculated using the distances given in Cappellari et al. (2011a) and references therein.

Galaxy	Obs. time (s)	Obs. date	Pointings	R_{max}/R_e	R_{max} (kpc)
NGC 680	9000	2011 January	1	3.5	9.3
NGC 1023	39600	2011 January	2	1.9	4.9
NGC 2685	44100	2011 January	2	2.5	5.2
NGC 2764	81000	2010 March	1	2.9	6.9
NGC 3522	12600	2011 January	1	3.0	3.8
NGC 3626	21600	2011 April	1	2.9	6.9
NGC 3998	66600	2010 March	1	2.8	3.7
NGC 4203	12600	2010 June	1	1.9	3.9
NGC 5582	59400	2010 June	1	1.9	7.1
NGC 5631	25200	2011 April	2	2.9	7.8
NGC 6798	21800	2010 June	1	2.9	8.9
UGC 03960	18000	2011 January	1	2.6	7.3

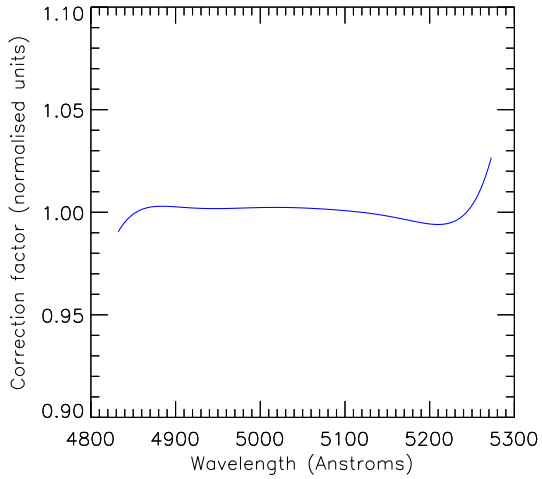

Figure 3. Polynomial SAURON-to-SDSS correction curve obtained for NGC 3522 over the wavelength range of the reduced ATLAS^{3D} data cube (4825–5280 Å). The curve is near flat, and so we conclude that the SDSS and ATLAS^{3D} data have consistent flux calibration for this galaxy.

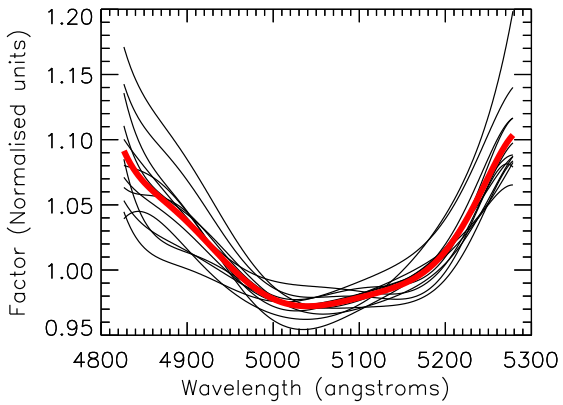

Figure 4. Mitchell-to-SAURON flux-calibration curves (black lines) calculated for all galaxies in normalized units. The thick red line shows the average curve. The calculated curves are broadly similar, though a degree of scatter is evident. The root-mean-square scatter from the mean is at most 4 per cent.

window of Fig. 5. We find that, while the calibration is improved significantly, the ATLAS^{3D} and Mitchell curves still show significant offsets on the blue end.

We therefore derive an additional correction factor by fitting a seventh-order polynomial to the *average* Mitchell-SAURON calibration offset, while forcing the polynomial to approach unity at wavelengths redder than the SAURON wavelength range. We apply this polynomial curve to the Mitchell-to-SDSS curve found previously, thus obtaining a final flux-calibration curve that we apply to all spectra for our galaxies. We show the resulting Mitchell-to-SAURON calibration curves in the right-hand side of Fig. 5. The mean calibration curve is consistently below 1 per cent, with the root-mean-square (rms) scatter from the mean at most 4 per cent.

3 KINEMATICS

In this section, we describe the extraction of line-of-sight kinematics for our ETG sample. We extract stellar kinematics up to the fourth Gauss-Hermite moment, and we quantify the angular momentum of the galaxies as a function of position. We also measure fluxes and line-of-sight kinematics of the ionized gas components in order to clean our spectra of emission. We present our stellar kinematics in Section 3.1 and we compare them with ATLAS^{3D} in Section 3.2. We quantify the galaxies' angular momentum in Section 3.3, and we present the calculation of ionized gas fluxes and kinematics in Section 3.4.

3.1 Stellar kinematics

We extracted stellar kinematics using the PYTHON implementation of the publicly available penalized PiXel Fitting (PPXF) software of Cappellari & Emsellem (2004)[1], which includes the upgrade described in Cappellari (2017). The PPXF routine recovers the line-of-sight velocity distribution (LOSVD) by fitting an optimized template $G_{mod}(x)$ to an observed galaxy spectrum directly in pixel space after logarithmically rebinning the spectrum in the wavelength direction. For our implementation, we added the derived sky spectra back into our galaxy spectra and then performed a second sky

[1] Available from http://purl.org/cappellari/software.

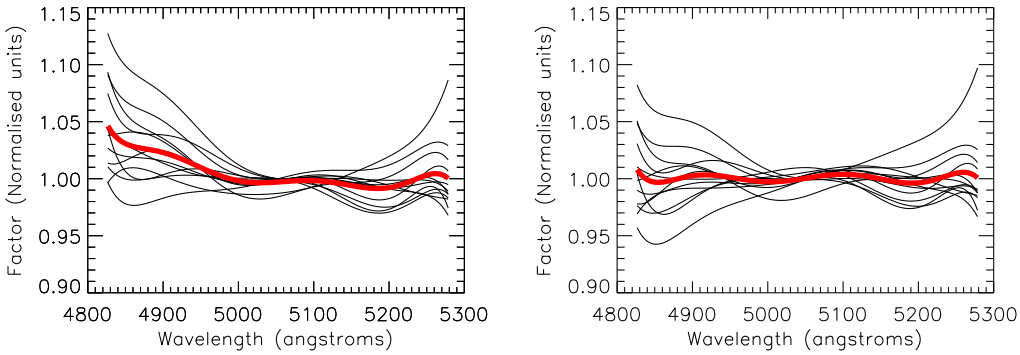

Figure 5. Mitchell-to-SAURON flux-calibration curves, with all lines as in Fig. 4. In the left-hand side, we have applied to the Mitchell data the Mitchell-to-SDSS correction curve obtained for NGC 3522. In the right-hand side, we have further applied the Mitchell-to-SAURON correction curve discussed in the text. The calibration between the two instruments is significantly improved by our flux-calibration procedure.

subtraction in PPXF in order to improve the subtraction in the sky-dominated outskirts of our FOV (e.g. Weijmans et al. 2009). The model spectra therefore take the form

$$G_{\rm mod}(x)=\sum_{k=1}^{K} w_k[\mathcal{L}(cx) * T_k](x)+\sum_{l=0}^{L} b_l \mathcal{P}_l(x)+\sum_{n=1}^{N} s_n S_n(x), \quad (1)$$

where $\mathcal{L}(cx)$ is the broadening function, T_k is a set of distinct stellar templates and w_k is the optimal weights of those templates, with $*$ describing convolution. $\mathcal{P}_l(x)$ are Legendre polynomials of order l, with b_l the corresponding weights; these are used to adjust for low-frequency differences between model and data. Likewise, s_n and S_n are the optimal sky weights and the sky templates themselves, respectively. For a given galaxy, the sky templates consist of all sky observations taken as part of that galaxy's observing run.

In this case, we have allowed for a 10th-degree additive Legendre polynomial correction. An alternative would be to instead use a multiplicative polynomial correction. However, such a correction is limited by the input stellar templates, and so is less free to account for low-frequency residuals when compared to an additive correction; as such, we prefer using an additive correction when deriving stellar kinematics.

The PPXF routine makes use of an input 'bias parameter, which prevents spurious solutions by biasing the recovered LOSVD towards a perfect Gaussian when h_3 and h_4 become ill- determined. It is important to select this parameter accurately: too high a value will bias the kinematics towards a Gaussian distribution even when h_3 and h_4 could be determined accurately, while too low a value risks overfitting of noisy data. We therefore optimized the bias parameter using the simulation code included in the PPXF package, with the standard prescription that the deviation between input and output h_3 and h_4 should be less than rms/3 for values of σ greater than three times the velocity scale. This led to an optimal bias of 0.2 for our target S/N of 20.

For stellar templates, we used stellar templates from the full medium resolution (FHWM = 0.51 Å) ELODIE library (Prugniel & Soubiran 2001) of observed stars. It is computationally expensive to fit the full library to each individual spectral bin; we therefore selected templates from the library by binning each galaxy into a series of elliptical annuli using the global ellipticities and position angles derived in Krajnović et al. (2011) from SDSS and INT imaging data; we performed PPXF fits on these annuli using the full ELODIE library, and we selected any star that was given a non-zero weight. We then ran PPXF over all galaxy spectra with the emission line regions (H β, [O III] and [N I]) masked out, while iteratively detecting and masking bad pixels; we also masked the red and blue edges of all spectra when fitting to avoid any potential problems relating to flat-fielding. We show some example PPXF fits in Fig. 6, and we present the resulting line-of-sight kinematics in Figs 7–10.

We determined random measurement errors by adding Gaussian noise to the spectra and re-running the fits with zero bias for 100 iterations each. However, these errors alone do not consider systematic effects – such as template mismatch and imperfect sky subtraction – and so will underestimate the true level of uncertainty (e.g. Arnold et al. 2014). We estimate the level of systematic error in a similar manner to Boardman et al. (2016). We derive PPXF kinematics using the MILES library of observed stars Sánchez-Blázquez et al. (2006) in the same manner as above, after broadening our spectra to match the MILES library resolution of 2.51 Å (Falcón-Barroso et al. 2011). We compute the residuals between the derived kinematics, and we then calculate the 1σ dispersion between the residuals with respect to zero. We derive systematic error values of 3.3 km s^{-1}, 4.3 km s^{-1}, 0.03 and 0.04 for the velocity, dispersion, h_3 and h_4, respectively, which we add in quadrature to the original errors; this results in median overall error values of 4.1 km s^{-1}, 5.7 km s^{-1}, 0.04 and 0.05, respectively.

We compare the kinematics from ELODIE and MILES templates in Fig. 11. Our findings are essentially identical to what was previously reported for NGC 3998 in Boardman et al. (2016): we find 1–1 agreement in the velocity, h_3 and h_4 values – albeit with non-negligible levels of scatter – but we find that the MILES results tend towards higher dispersion values when the ELODIE velocity dispersion is low. We view the ELODIE results as being more reliable in such cases due to the MILES library's higher intrinsic dispersion of $\sim$60 km s^{-1}, which is above what we find with ELODIE in most of the galaxies' outskirts. For ELODIE dispersions below 60 km s^{-1}, the derived MILES dispersion is 5.5 km s^{-1} higher on average.

We assessed the level of systematic error due to imperfect sky subtraction, by comparing the kinematics described above to two sets of kinematics obtained after oversubtracting and under-subtracting the sky by 10 per cent, respectively. For each of these new kinematic data sets, we compare to the original kinematic data set and then calculated systematic errors in the same manner described previously. This led to maximum systematic error values of 1.7 km s^{-1}, 1.7 km s^{-1}, 0.02 and 0.02 for velocity, dispersion, h_3 and h_4, respectively; these values are small compared to the sources of error already considered, so we do not factor these into our error calculation.

We also derived PPXF kinematics for the first two moments (V, σ) only, for use in cases where the higher-order moments are not

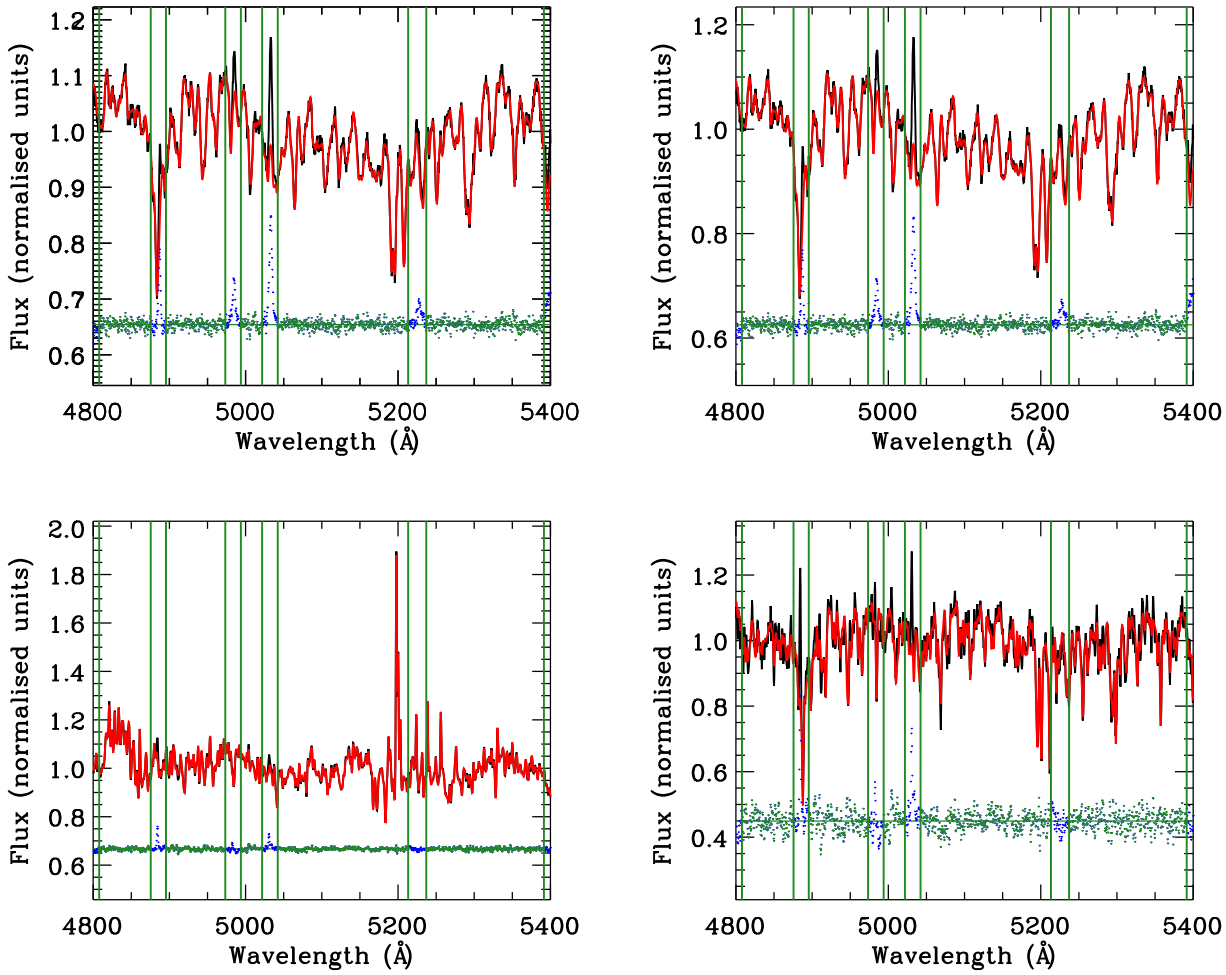

Figure 6. Example PPXF fits of high-signal (top) and sky-dominated (bottom) spectra from NGC 3626, before (left) and after (right) PPXF has been used to subtract the sky. Black lines show the observed spectra and red lines show the best-fitting superposition of templates. Vertical green lines indicate regions that we excluded from the fit, green dots indicate the fit residuals and blue dots indicate the residuals over excluded regions. The sky provides an insignificant contribution to the top spectrum, while for the bottom spectrum PPXF is able to fit and subtract the dominant sky component.

required; this is to prevent any dependence on h_3, h_4 or the PPXF penalty parameter in cases where only the first two moments are needed. We obtained errors in the same way as before, deriving systematic error terms of 5.9 and 8.2 km s^{-1} for the velocity and velocity dispersion in turn; this produces median overall error values of 6.5 and 9.1 km s^{-1}.

3.2 Comparison with ATLAS^{3D}

As all of our galaxies form part of the ATLAS^{3D} survey, it is useful to compare our kinematics with those derived previously with the SAURON instrument. We first perform this comparison by finding all Mitchell spectra for which an ATLAS^{3D} bin lies within the radius of a Mitchell fibre (2.08 arcsec); we then compare the kinematics of these bins with those of the closest ATLAS^{3D} bin. We compare the velocities and dispersions calculated from two-moment PPXF fits, as well as the kinematics calculated from four-moment fits. We found excellent agreement in the line-of-sight velocities calculated between the two data sets; however, we also found the ATLAS^{3D} velocity dispersions to be systematically higher on average when fitting for h_3 and h_4, while the h_3 and h_4 comparisons show a high degree of scatter.

There are several potential confounding factors in this comparison, however. The ATLAS^{3D} spectra for our galaxies have an instrumental dispersion of $\sigma_{\rm instr} \approx 98$ km s^{-1}, and we find many galaxies to have dispersions below this even within the area covered by ATLAS^{3D}. In addition, the ATLAS^{3D} data cubes are often significantly binned towards the edge of their FOV, which could serve to artificially enhance the measured dispersion (e.g. Arnold et al. 2014). Lastly, the Mitchell fibres are significantly larger than the 0.8 arcsec × 0.8 arcsec spaxels employed by ATLAS^{3D}.

Motivated by the above, we performed a second comparison in the following way. We first selected data points to compare in the same manner as before. We then excluded any data points for which the Mitchell spectrograph velocity dispersion was below 98 km s^{-1}, and we further excluded data points for h_3 and h_4 for which the Mitchell dispersion was below 120 km s^{-1}; this is to ensure that the dispersion could be accurately measured in ATLAS^{3D} without strong penalization of h_3 or h_4. We further limited ourselves to data points in which neither the Mitchell nor the ATLAS^{3D} spectra had been binned, in order to ensure that the velocity dispersion in one or both data sets was not being enhanced by binning. We show the results of this in Fig. 12, along with the results of the first comparison discussed previously. We now find excellent agreement

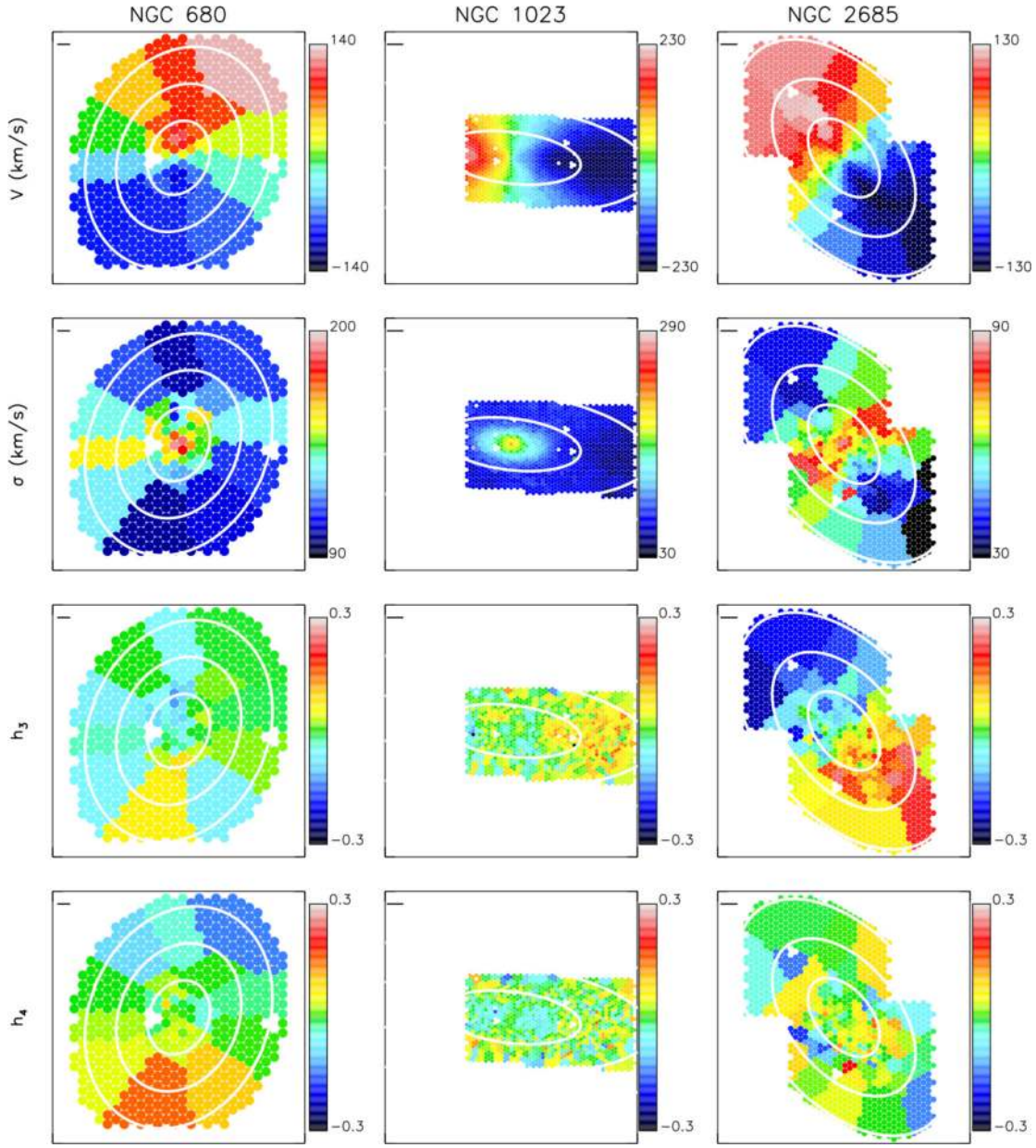

Figure 7. Kinematics maps for NGC 680, NGC 1023 and NGC 2685. Rows from top to bottom: velocity ($\mathrm{km\,s^{-1}}$), velocity dispersion ($\mathrm{km\,s^{-1}}$), h_3, h_4. The solid black lines mark a length of 1 kpc. The white contours are spaced in units of R_e. Fibre positions from the missing NGC 2685 dither on the top left of our FOV have been re-added for presentational purposes, with kinematics assigned to each from the nearest Voronoi bin.

between the velocity and dispersion of the two data sets, though the h_3 and h_4 comparisons continue to show a large degree of scatter.

We present one final comparison in Fig. 13. Here, we take each Mitchell kinematic data point in turn and find all SAURON data points within the Mitchell fibre radius, and then compare each Mitchell data point to the selected SAURON data point that is *closest in value* to the Mitchell data point being considered. Unbinned high-dispersion data points were selected in the same manner as described previously. We find tight one-to-one relations with almost no scatter in this case, once data point affected by binning or low dispersions have been excluded. We therefore find our data to be fully consistent with that from the ATLAS^{3D} survey.

3.3 Stellar angular momentum

We tested our stellar kinematics for transitions beyond $1R_e$, by considering the galaxy angular momentum as a function of radius. We explore the angular momentum of the galaxies by using the λ_R parameter (Emsellem et al. 2007) as proxy, which in the case of two-dimensional spectroscopy takes the form

$$\lambda_R = \frac{\langle \sum_{i=1}^{N_P} F_i R_i |V_i| \rangle}{\langle R \sum_{i=1}^{N_P} F_i R_i \sqrt{V_i^2 + \sigma_i^2} \rangle}, \quad (2)$$

where R signifies the mean radius of an ellipse, F represents the flux, V is the line-of-sight velocity and σ the velocity dispersion. We calculate λ_R, by summing over all fibres for which the centre falls within a given ellipse, after applying to each fibre the kinematics

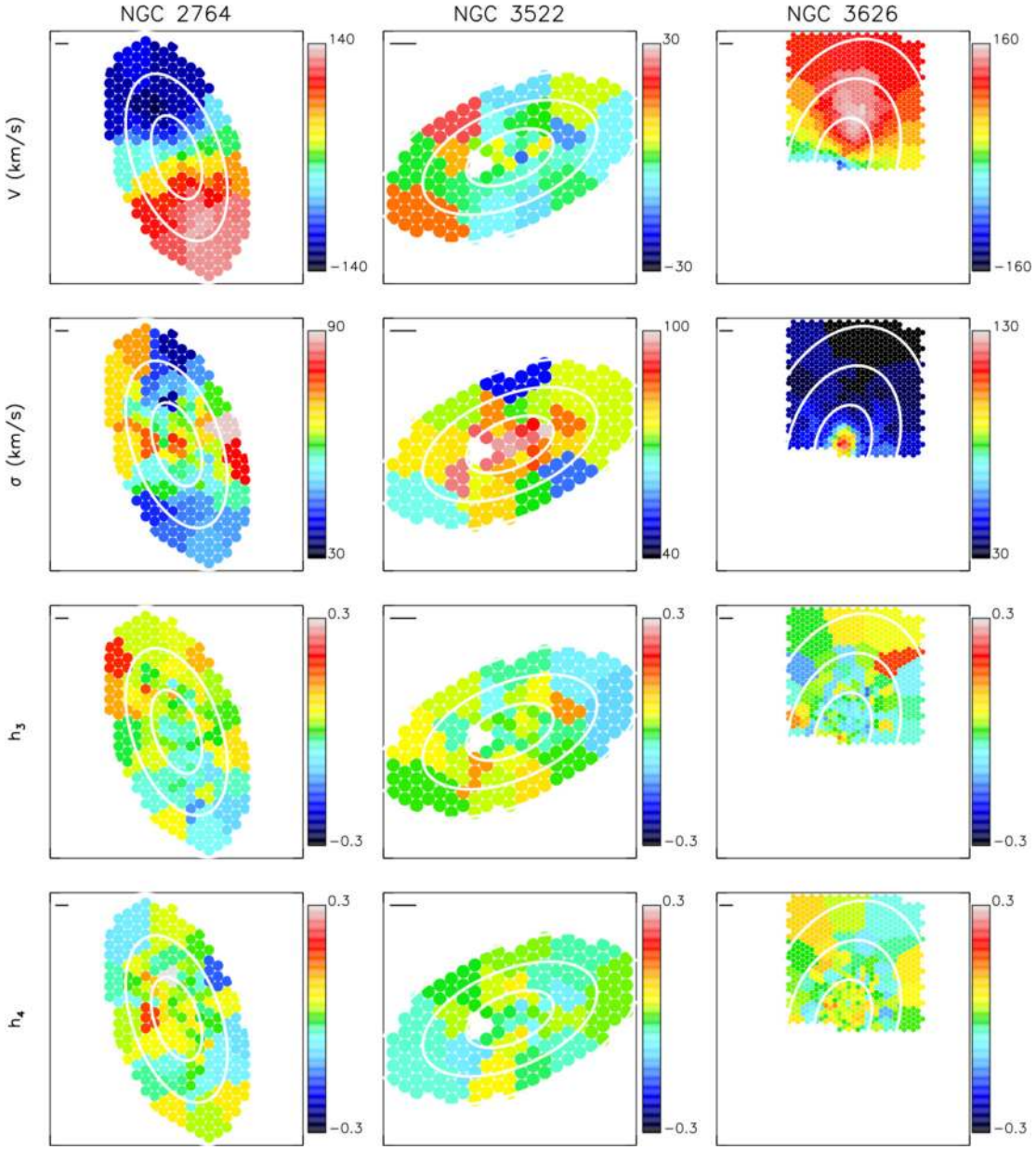

Figure 8. Same as in Fig. 7, but for galaxies NGC 2764, NGC 3522 and NGC 3626.

of its corresponding Voronoi bin. We do not attempt to calculate the profiles beyond $R = R_{\rm max}$ to ensure that the ellipse is always well filled with spectra. We used velocities and dispersions from the PPXF fits to V and σ only. We symmetrized the kinematics and fibre positions when calculating λ_R for NCG 1023 and NGC 3626, replicating the kinematics values on the missing sides, due to these galaxies not being centred on our FOV. We used ellipses of constant ellipticity, based on the global ellipticities and position angles for these galaxies reported in Krajnović et al. (2011).

We present λ_R profiles for our sample in Fig. 14. We find no clear transitions in the galaxies' angular momentum beyond the central effective radius: beyond $1R_e$, galaxies in our sample show the expected slightly rising or rather constant λ_R profiles. Hence, galaxies that are FRs (SRs) at $1R_e$, following the Emsellem et al. (2011) definitions, keep their high (low) λ_R profiles over the full FOV relative to their respective ellipticities. All but one of our galaxies show slightly rising λ_R profiles overall; the exception here is NGC 5631, which is a known kinematically decoupled core, with isophotes becoming nearly round at large radii and with an associated expected decline in its λ_R profile.

3.4 Ionized gas kinematics

We extracted ionized gas fluxes and kinematics using the GANDALF code of Sarzi et al. (2006), with the aim of cleaning our spectra of emission.

Previously, we ran PPXF allowing for an *additive* Legendre polynomial correction. Such a correction can produce unrealistic features in model spectra over masked wavelength regions, due to the correction's lack of dependence on the stellar templates; this makes an additive correction ill suited for extracting ionized gas emission lines. We therefore re-ran PPXF allowing for a 10th-degree

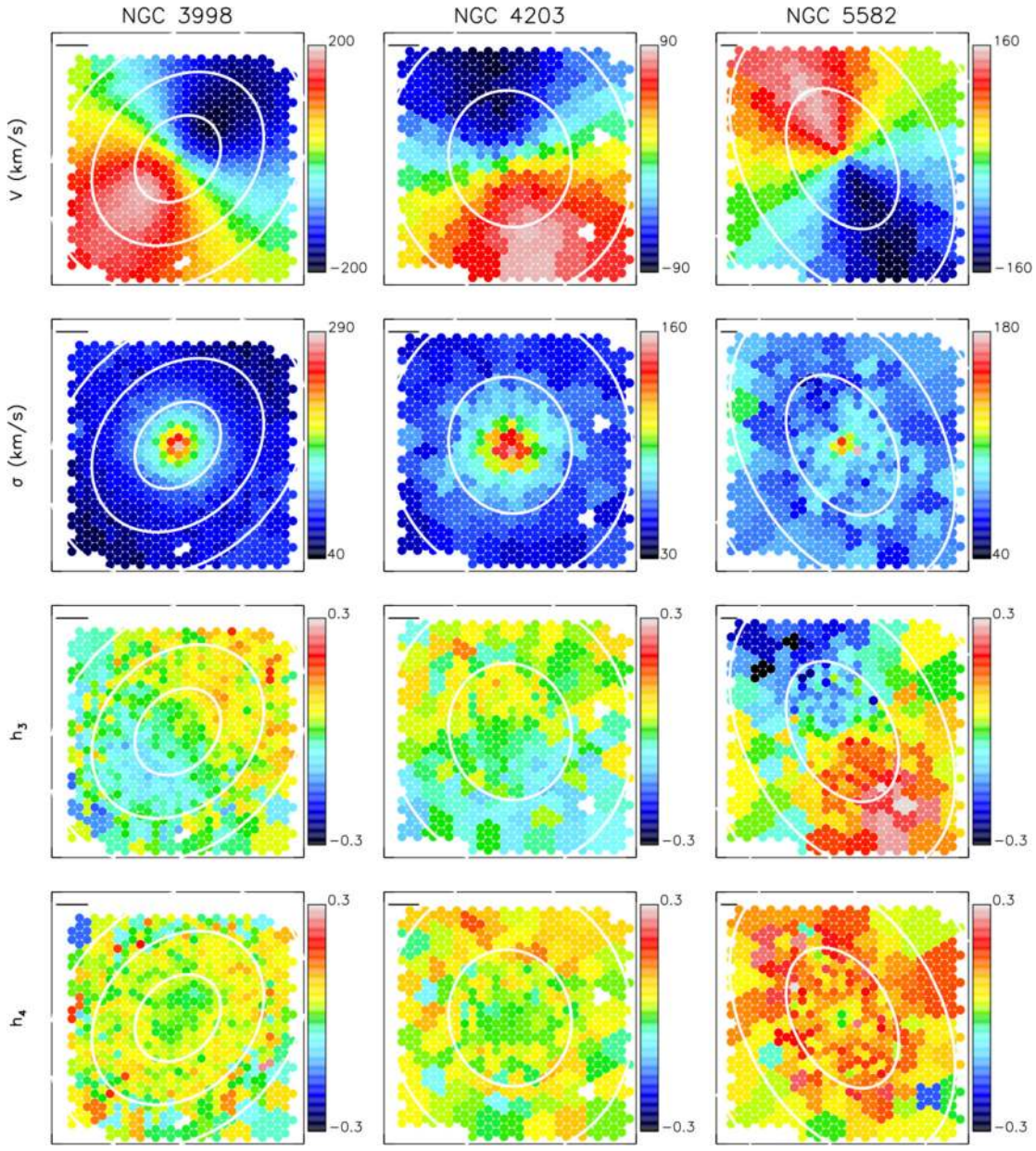

Figure 9. Same as in Fig. 7, but for galaxies NGC 3998, NGC 4203 and NGC 5582. Fibre positions from the missing NGC 4203 dither have been re-added for presentational purposes, with kinematics assigned to each from the nearest Voronoi bin.

multiplicative Legendre polynomial instead, which accounts for residual continuum variation while avoiding degeneracies with individual line strengths. We again used PPXF to fit and subtract the sky, therefore obtaining model galaxy spectra of the form

$$G_{mod}(x) = \sum_{k=1}^{K} w_k[\mathcal{L}(cx) * T_k](x) \times \sum_{l=1}^{L} b_l \mathcal{P}_l(x) + \sum_{n=1}^{N} s_n S_n(x) \quad (3)$$

in which all symbols are as before. We derive systematic error terms by recalculating the kinematics with MILES stars as before, finding values of 3.1 km s^{-1}, 4.7 km s^{-1}, 0.03 and 0.04 for each kinematic moment in turn.

The GANDALF code uses the PPXF-derived stellar kinematics as inputs in order to derive a new optimal stellar template along with an accompanying optimal emission template. Flux values are calculated for each emission line, along with the first two kinematic moments (V, σ).

We implemented GANDALF as follows. We again allowed for a 10th-order multiplicative Legendre polynomial correction to account for continuum variation. We searched for three ionized gas features in each of our spectra: H β line, the [O III] doublet and the [N I] doublet. We performed an initial GANDALF fit for each binned spectrum in which the H β and [N I] emission regions were masked to derive kinematics for the [O III] emission; afterwards, we fit for all expected emission features with the gas kinematics fixed to the [O III] value. We calculated for each spectrum the amplitude-over-noise (A/N) ratio of all detected features in the fit. We then extracted all [O III] features with A/N $>$ 4 and we extracted all H β and [N I] features with A/N $>$ 3, following the reasoning in Sarzi et al. (2006). We present an example GANDALF fit in Fig. 15. We applied the GANDALF-derived continuum correction to each of our spectra

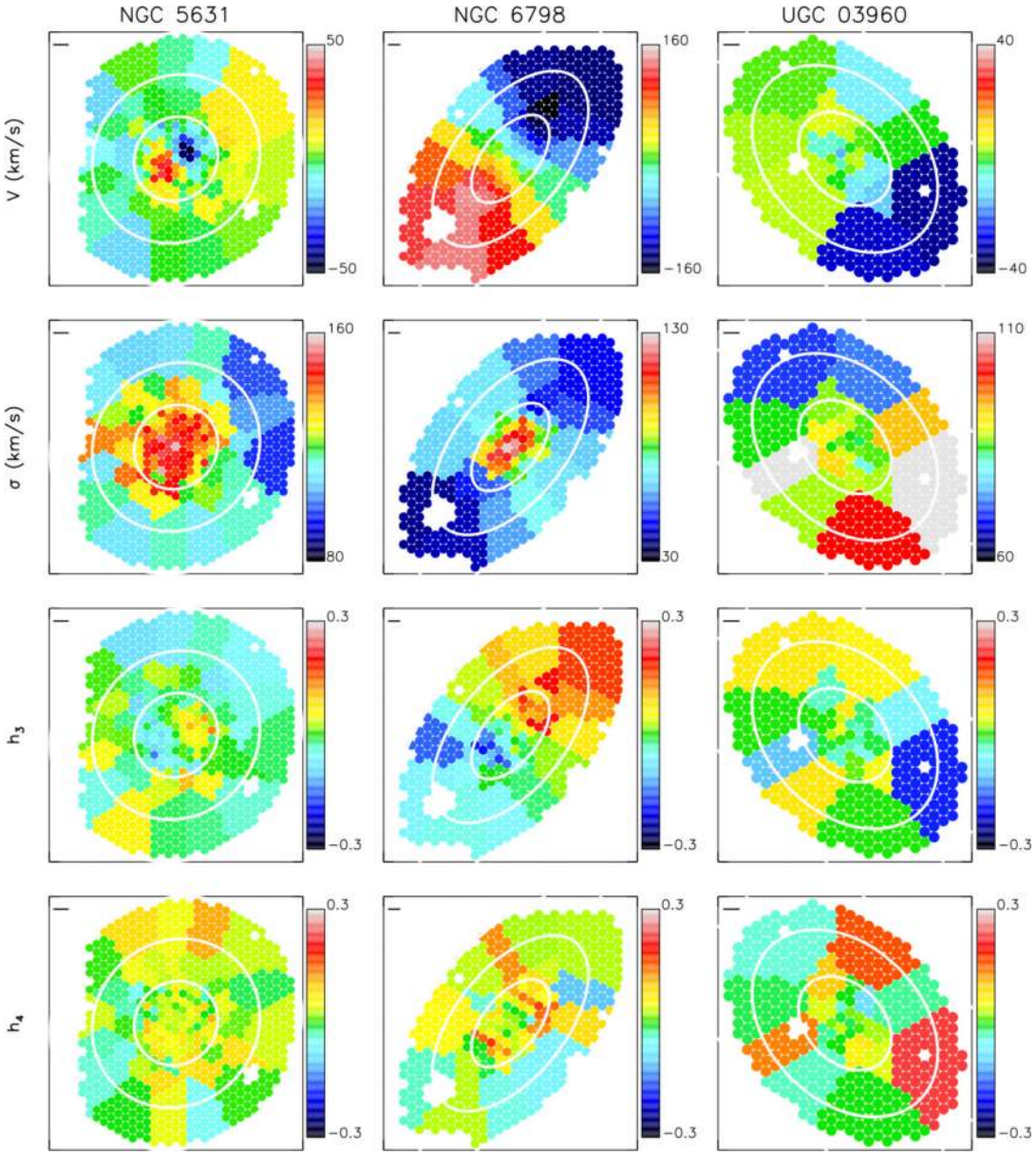

Figure 10. Same as in Fig. 7, but for galaxies NGC 5631, NGC 6798 and UGC 03960.

before proceeding in order to account for any residual continuum contamination.

Although the above procedure produced good fits for the vast majority of spectra in our sample, we noted significant fit residuals around the H β region over much of the FOV for NGC 2764. Given that H β is the only age-sensitive stellar absorption feature within the wavelength range of our data, we exclude NGC 2764 from the stellar population analysis described in Section 5.

We present our extracted [O III] fluxes and velocities in Figs 16 and 17. We detect ionized gas well beyond the central effective radius for many of our galaxies. We observe several cases in which the ionized gas is counter rotating or else misaligned with respect to the stars; we demonstrate this in Table 3, in which we calculate the misalignment angles using the method described in appendix C of Krajnović et al. (2006).[2] The latter point is not a new result for these systems, being already apparent from the SAURON gas maps published by ATLAS^{3D} (Davis et al. 2011), but is relevant when considering these galaxies' evolutionary pasts.

[2] Available from http://purl.org/cappellari/software.

4 LINE STRENGTHS

In this section, we describe the extraction of absorption line strengths for our galaxy sample, which we will then use to constrain the stellar ages, metallicities and abundance ratios of these galaxies. Each index consists of a central bandpass, where the absorption feature is located, along with a pair of blue and red pseudocontinua. An index is measured by determining the mean of each pseudo-continuum and then drawing a straight line between the two midpoints; the index is then given by the difference in flux between the central bandpass and the line (Worthey et al. 1994).

We begin by broadening all of our spectra to the 14 Å line–index system (LIS) proposed in Vazdekis et al. (2010), in which spectra

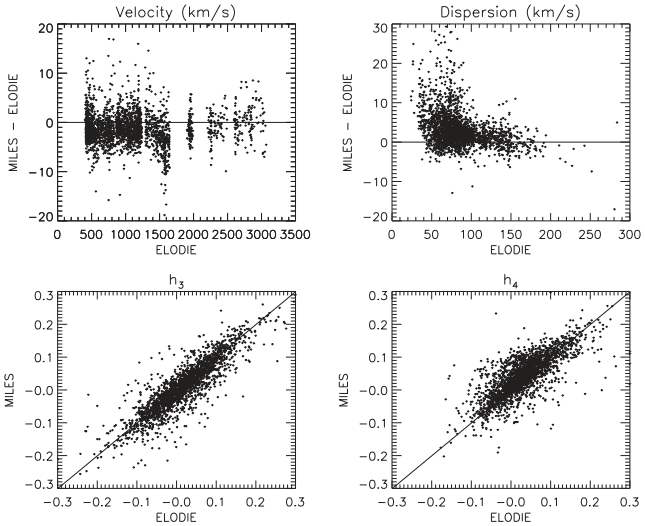

Figure 11. Comparison of Mitchell kinematics for our 12 galaxies derived using ELODIE and MILES libraries in PPXF. We show absolute values of h_3 and h_4 from both ELODIE and MILES libraries, while we show the relative differences between ELODIE and MILES velocities and dispersions in order to emphasize differences. We find good overall agreement in the velocity, h_3 and h_4 values, though with non-negligible scatter. We also find that the MILES dispersion values approach larger values when the ELODIE value is low, which we argue to be due to the MILES library's higher intrinsic dispersion.

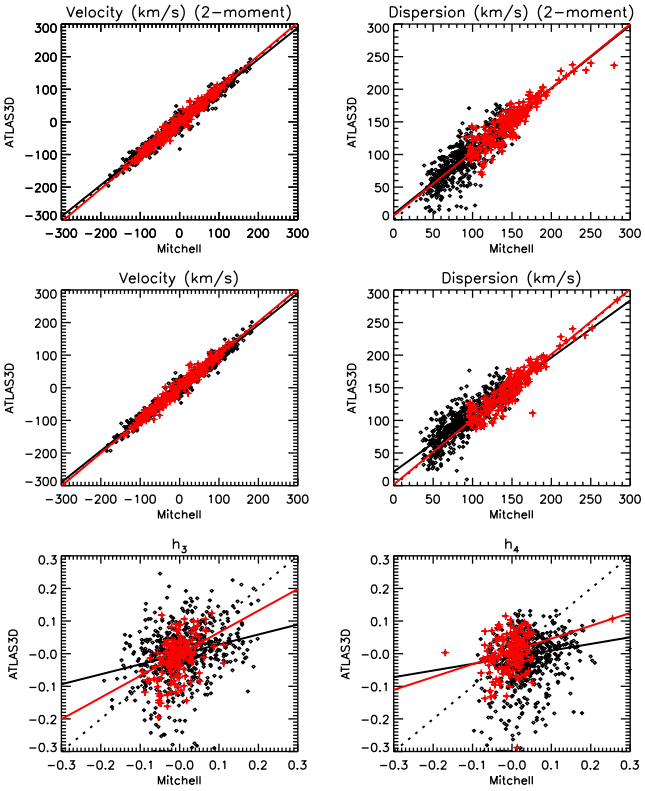

Figure 12. Comparison of the Mitchell kinematics of our twelve galaxies with the kinematics reported in ATLAS^{3D}. The dotted lines show the one-to-one relation, while the solid lines are obtained from a robust least-absolute-deviation fit. Unbinned high-dispersion data points are highlighted with red crosses; the red solid lines show robust least-absolute-deviation fits to these points. We find that significantly improved consistency with ATLAS^{3D} once low-dispersion and/or binned data points are excluded.

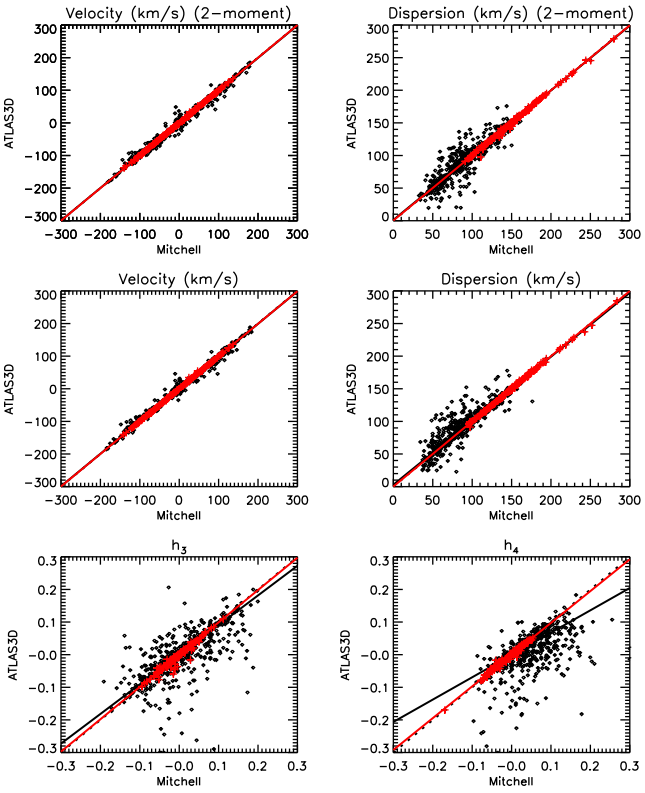

Figure 13. Same as in Fig. 12, except that the Mitchell data points have been matched to the SAURON data point within 2.08 arcsec that is *closest in value*. All lines and symbols are as before. We find one-to-one agreement once low-dispersion and binned data points have been removed, with very little scatter.

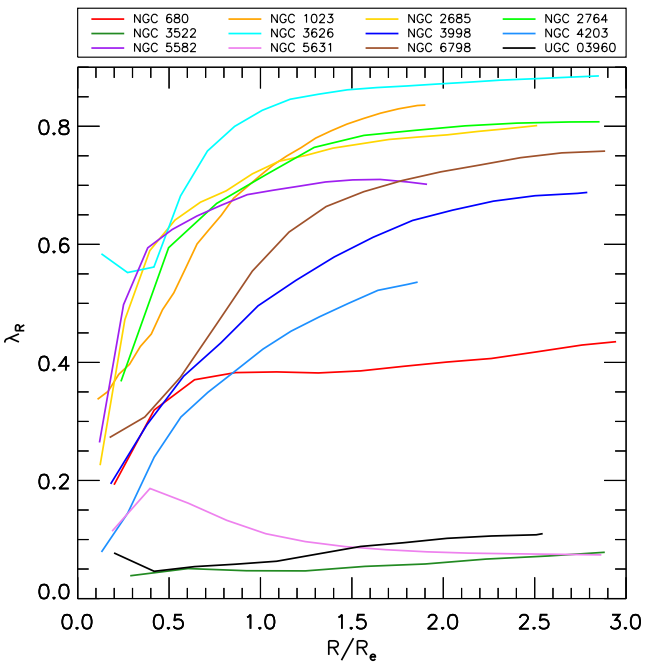

Figure 14. λ_R profiles for our 12 ETGs. We find no abrupt drops beyond the central half-light radius, with all but one galaxy (NGC 5631) showing rising profiles overall.

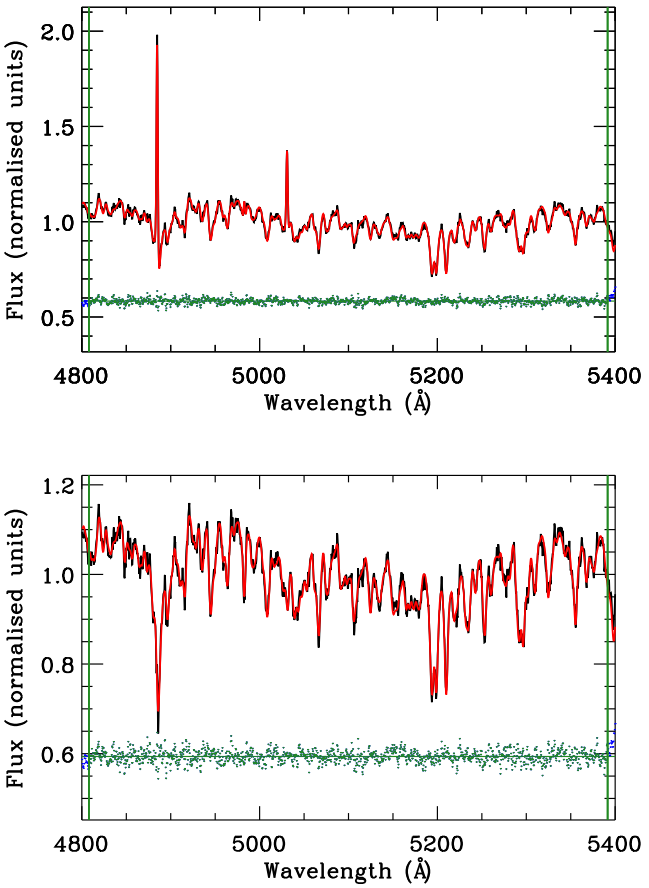

Figure 15. Example GANDALF fit to a sky-subtracted galaxy spectrum from NGC 3626, before (top) and after (bottom) subtracting the GANDALF-derived emission component. All lines are same as in Fig. 6.

are broadened to a constant FWHM of 14 Å. We take both the instrumental dispersion and stellar velocity dispersion into account when broadening, resulting in spectra with an FWHM of 14 Å independent of wavelength. We then calculate line indices for each of our spectra, using the PPXF-derived stellar velocities to determine the required amount of redshifting. We calculate the H β, Fe5015, Mg b and Fe5270 indices for all galaxies. We also calculate the Fe5335 index where possible; we are not able to calculate this index for all objects, as its red continuum region is redshifted beyond the available wavelength range in certain cases.

We calculate errors by performing 500 Monte Carlo re-simulations, with Gaussian noise added to the spectra and to the input PPXF line-of-sight velocities. We set lower limits on the errors by calculating the differences between the indices from a given spectrum and those from the associated optimal template, likewise broadened to 14 Å FWHM; in practice, this means that the errors in the inner parts of each galaxy are set by data-template differences, whereas further out we find random errors to dominate. We present two-dimensional maps of the line indices for our sample in four supplementary figures available online.

For visualization purposes, we construct smoothed line index profiles as follows. We place over each galaxy a central elliptical aperture and three elliptical annuli; the central apertures have a major axis radius of $0.5R_e$, while the annuli have major-axis boundaries at $0.5R_e$, $1R_e$, $1.5R_e$ and $2.5R_e$. We discounted the outer annulus for galaxies with $R_{\rm max} < 2.5$ to ensure good coverage for all annuli. We obtain the associated line index value across all of the resulting regions by taking the mean of all Voronoi bins whose light-weighted centres fall within each annulus.

We present the resulting H β and Mg b profiles in Fig. 18, in which radii are given as flux-weighted average radii for a given aperture or annulus. We find a wide range of H β behaviours: the majority of our galaxies show flat H β profiles, but we also find H β to rise or fall in individual systems. We observe steep H β rises for the galaxies NGC 2685 and NGC 6798, while we see significant falls for the galaxies NGC 2764 and NGC 3626. We find Mg b to fall with radius for most of our galaxies; the two exceptions here are NGC 2764 and NGC 3626, for which the Mg b gradient is near flat.

In Fig. 19, we assess the well-known Mg $b - \sigma$ correlation out to multiple effective radii. We take an elliptical aperture of major axis radius $0.5R_e$ along with two elliptical annuli with boundaries at $0.5R_e$, $1R_e$ and $2R_e$. We take the mean of all relevant Voronoi bins as before in each case, with errors propagated accordingly. Performing least-absolute-deviation fits to our data, we find gradients Δ(Mg b)/dex of 3.9, 2.6 and 4.0, respectively. We therefore find that the Mg b–σ relation holds beyond the central effective radius for our sample. The changing gradients of our straight-line fits are largely driven by the galaxies NGC 2764 and NGC 3626, which both have flat Mg b gradients and low Mg b values; if we exclude these two galaxies, we obtain gradients of 4.2, 4.0 and 4.1 from the straight-line fits.

5 STELLAR POPULATION MODELLING

In this section, we use our emission-cleaned spectra to calculate ages, metallicities [Z/H] and abundance ratios for our sample of galaxies, with NGC 2764 excluded as discussed previously. We perform full spectral fitting of the gas-cleaned spectra using PPXF, thereby making full use of the information offered by the spectra.

We de-redshifted the galaxies' spectra and then combined them into a series of central apertures and elliptical annuli in order to ensure sufficiently high S/N when performing the fit. We used ellipticities equal to the global ellipticity for each galaxy, with aperture/annulus boundaries at $0.5R_e$, $1R_e$, $1.5R_e$ and $2.5R_e$; for each aperture or annulus, we then combine all Voronoi-binned spectra for which the luminosity-weighted centre falls within the annulus. We discounted the outer annulus for galaxies with $R_{\rm max} < 2.5$. We then cleaned the combined spectra of *all* detected gas emission rather than using the A/N limits discussed previously. This is because the detected emission often went below the conventional A/N limits at the edges of our FOV, resulting in significant under-subtraction of the emission (and so notable residuals in the PPXF fits) when the spectra were combined.

We performed spectral fitting on the combined spectra by using PPXF to fit linear combinations of Simple Stellar Population (SSP) models from the MILES SSP library (Vazdekis et al. 2010). We used the solar-scaled ([α/Fe] = 0) and alpha-enhanced ([α/Fe] = 0.4) MILES models presented in Vazdekis et al. (2015), spaced approximately logarithmically in age and metallicity. We did not use exact log-spacing for age and metallicity, due to the models themselves not being available with such spacing. We used model ages of 0.5, 0.7, 1, 1.5, 2.25, 3.25, 4.5, 6.5, 9.5 and 14 Gyr; we used model metallicity [Z/H] values meanwhile of −2.27, −1.79, −1.49, −1.26, −0.96, −0.66, −0.35, 0.06 and 0.4. We also tracked the stellar mass M_* and luminosity L_V for each model, where M_* includes

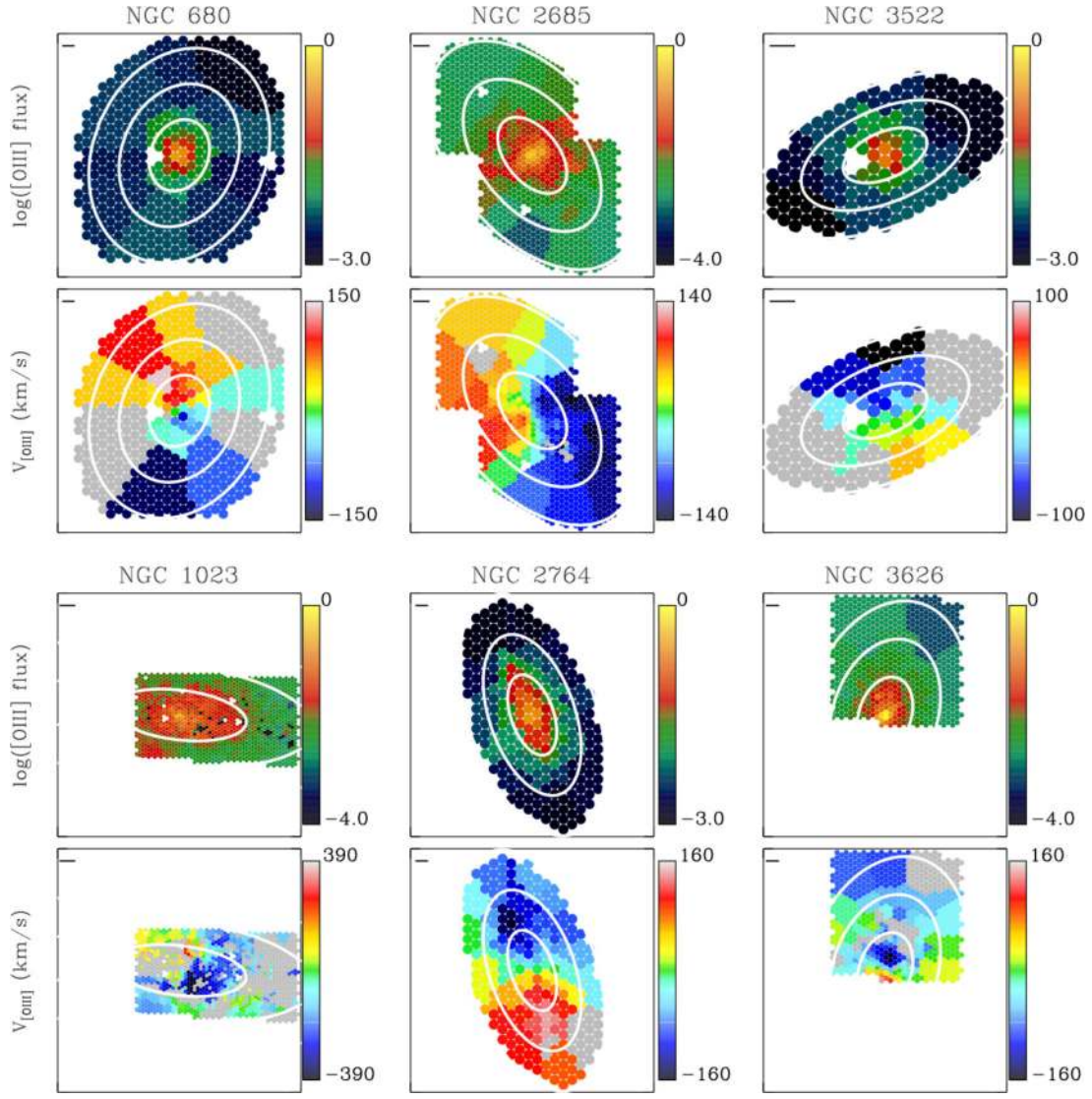

Figure 16. Maps of log(O III flux) (top, arbitrary units) and O III velocity (bottom, km s^{-1}) for the first six galaxies in the ETG sample. Flux is in arbitrary units and has been divided through by the number of fibres comprising each spectral bin. Grey bins in the velocity maps indicate regions below our amplitude-over-noise threshold, as discussed in the text. The white contours are spaced in units of R_e. The solid black lines in the top left corner mark a length of 1 kpc. Fibre positions from the missing NGC 2685 dither on the top left of our FOV have been re-added for presentational purposes, with kinematics and fluxes assigned to each from the nearest Voronoi bin.

the mass of stellar remnants but excludes the gas lost during stellar evolution in order to derive a mass-to-light ratio (M_*/L_V) for each combined spectrum.

We allowed for four kinematic moments in the fit, as well as a 10th-degree multiplicative polynomial. We used a PPXF penalty parameter of 0.2, as before. For certain galaxies, we noted sharp sky features in the combined spectra that PPXF had not previously been able to subtract out; we created narrow masks over these features in such cases. We did not broaden the spectra to match the MILES spectral resolution in this case, in order to avoid degrading our spectra unnecessarily: our combined Mitchell spectra will be broader than the MILES SSP templates already due to the stellar velocity dispersion, while the SSP templates are broadened as appropriate by PPXF as part of the PPXF fit.

The PPXF SSP fits enable us to detect multiple stellar population components, which in turn allows us to measure the star formation history (SFH) for each galaxy. Inferring the SFH from spectra is an intrinsically degenerate process; however, as multiple combinations of stellar population components can produce near-identical observations. We account for this degeneracy by imposing a regularization constraint, using the 'regul' keyword in PPXF in order to force the PPXF solution towards the maximum smoothness allowed by the data (see section 3.5 of Cappellari 2017, for details).

The amount of regularization is controlled by a single regularization parameter. We optimize this parameter for each combined spectrum in turn as follows. We first perform a PPXF fit with no regularization and scale the errors on our spectra such that $\chi^2 = N$, where N is the number of good pixels across the spectrum. We then choose the regularization parameter such that $\Delta\chi^2 \simeq \sqrt{2N}$, where $\Delta\chi^2$ indicates the difference in χ^2 values for the regularized and non-regularized fits. We derived errors on our stellar population values by performing 100 Monte Carlo re-simulations with added Gaussian noise, using zero regularization and zero penalty.

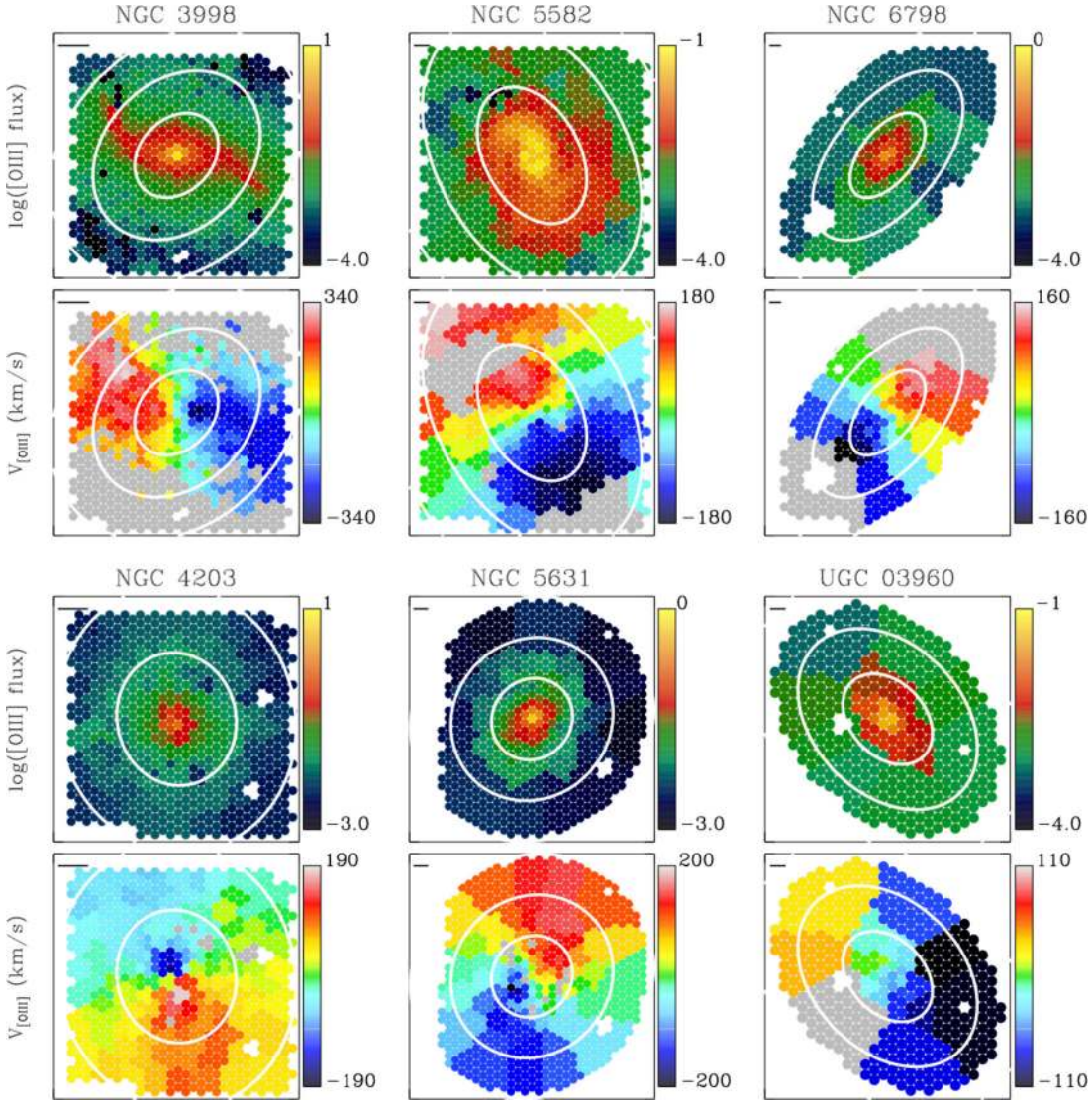

Figure 17. Same as in Fig. 16, for the remaining ETGs in the sample. Fibre positions from the missing NGC 4203 dither have been re-added for presentational purposes, with kinematics and fluxes assigned to each from the nearest Voronoi bin.

We calculated light-weighted and mass-weighted values for the age, metallicity and abundance ratio of each fitted model. The light- and mass-weighted value of a given parameter is then given by

$$X_{\rm mass} = \frac{\sum_{k=1}^{K} w_k \times x_k}{\sum_{k=1}^{K} w_k}, \quad (4)$$

$$X_{\rm light} = \frac{\sum_{k=1}^{K} w_k \times x_k \times F_k}{\sum_{k=1}^{K} w_k \times F_k}, \quad (5)$$

where x represents the parameter value of a given template, X is the final weighted value of that parameter, w_k is the template weights and F_k is the mean flux of each template across the Mitchell wavelength range. We use logarithms of the model ages when applying these equations, due to the logarithmic spacing employed for the SSP models. We calculated M_*/L_V using

$$M_*/L_V = \frac{\sum_{k=1}^{K} w_k \times M_{k,*}}{\sum_{k=1}^{K} w_k \times L_{k,V}}. \quad (6)$$

We compared the light-weighted stellar population parameters inferred from regularized and non-regularized PPXF fits, in order to verify that the parameters do not significantly depend on the regularization. We show the results of this comparison in Fig. 20. We find near one-to-one agreement overall between the two sets of values, though with a slight trend towards lower ages and higher metallicities. The fits to the outermost binned spectrum of UGC 03960 produce a significant anomaly in terms of age, with the non-regularized fit producing an age of 14 Gyr and the regularized fit yielding an age of 5.4 Gyr. This is caused by the non-regularized fit being at the edge of our model grid's parameter space, along with the relatively large degree of regularization applied to the regularized fit: the regularization increases the relative weights of young SSP models, thus lowering the light-weighted age.

In Fig. 21, we compare light-weighted and mass-weighted ages calculated for $1R_e$ apertures with the ATLAS^{3D} values reported in McDermid et al. (2015), along with the [Z/H] values inferred from our respective studies. The mass-weighted values in McDermid et al. (2015) were calculated using a very similar procedure to ours, though with MIUSCAT SSP models (Vazdekis et al. 2012) rather than MILES models. We compare our light-weighted values with values calculated from fits to absorption line indices, which used

Table 3. Stellar and ionized gas kinematic position angles and uncertainties of our ETG sample, measured anticlockwise from north for the receding part of the velocity map using the method of Krajnović et al. (2006), along with the misalignment angles between the two. We do not report ionized gas position angle for NGC 1023 due to this galaxy's higher irregular gas kinematics.

Galaxy	θ_*	$\theta_{\rm ion}$	$\lvert\theta_* - \theta_{\rm ion}\rvert$ (°)
NGC 680	359.5 ± 8.5	22.5 ± 10.3	23.0
NGC 1023	86.5 ± 1.5	N/A	N/A
NGC 2685	38.0 ± 3.8	88.5 ± 5.5	50.5
NGC 2764	196.5 ± 7.8	185.5 ± 13.0	9.0
NGC 3522	116.5 ± 89.8	181.0 ± 24.5	64.5
NGC 3626	343.0 ± 4.0	168.0 ± 4.8	175.0
NGC 3998	136.5 ± 2.0	87.5 ± 2.5	49.0
NGC 4203	194.5 ± 6.8	198.0 ± 5.8	3.5
NGC 5582	29.0 ± 3.3	30.5 ± 3.5	1.5
NGC 5631	132.5 ± 31.5	319.5 ± 6.5	173.0
NGC 6798	139.0 ± 7.8	310.5 ± 7.0	171.5
UGC 03960	33.5 ± 89.8	97.0 ± 39.8	57.2

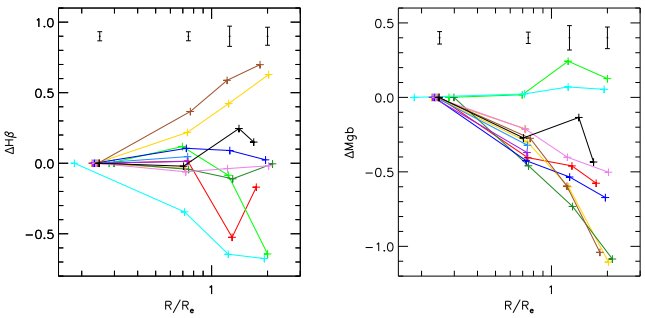

Figure 18. Relative H β and Mg b profiles for our ETG sample. We find declining Mg b profiles for most of our sample, but we find a wide range of H β behaviours. Lines are same as in Fig. 14.

Schiavon (2007) models. Our ages compare well with McDermid et al. (2015) and are consistent with a one-to-one relation; however, our light-weighted [Z/H] values are higher by an average of 0.13, while our mass-weighted [Z/H] is higher by an average of 0.32.

To test the effect of our choice of model library, we also performed PPXF fits to $1R_e$ apertures using SSP models from the MIUSCAT library. As in McDermid et al. (2015), we use a MIUSCAT model grid spanning a regular grid of log(age) and metallicity, using ages of 0.1–14 Gyr and metallicities [Z/H] of −1.71–0.22, giving 264 models in total. We optimize the amount of regularization in the same manner as described previously. We compare the results of these fits to the McDermid et al. (2015) values in Fig. 22. We find near one-to-one agreement in the galaxies' ages as well as in their light-weighted metallicity, though we obtain mass-weighted [Z/H] values that are higher on average by 0.08 with respect to ATLAS^{3D}. As such, the metallicity offsets seen in Fig. 21 appear to be largely due to our choice of SSP models.

We present profiles of light-weighted age and metallicity and [α/Fe] ratio in Fig. 23, in which the radius is given as the flux-weighted average radius for a given combined spectrum. We find negative metallicity gradients for all tested galaxies. We find age gradients that are negative on average, but detect a wide degree of variation between individual systems. NGC 3626 is particularly

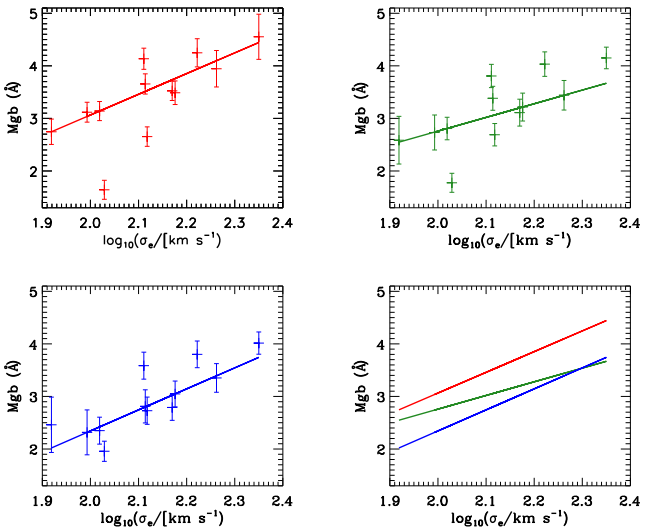

Figure 19. Mg b–σ relation computed over a $0.5R_e$ aperture (red; top left window), a 0.5–$1R_e$ annulus (green; top right window) and a 1–$2R_e$ annulus (blue; bottom left window). The thick lines show a least-absolute-deviation straight line fit for each set of points. The bottom right window shows the three straight line fits together. Values of σ_e, the velocity dispersion calculated over a $1R_e$ aperture, are taken from Cappellari et al. (2013b) and references therein. We find that the Mg b–σ relation holds over multiple effective radii in our sample.

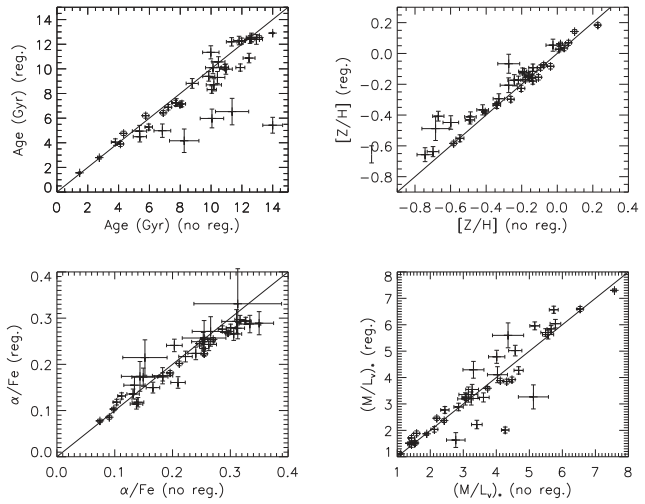

Figure 20. Comparison between stellar population parameters obtained from regularized and non-regularized PPXF fits, with black solid lines indicating one-to-one relations. We find good agreement between the two sets of fits, showing that our regularization scheme does not significantly affect the derived values.

notable, both due to its low central age and its strong positive age gradient. We note here that the age resolution of our model grid is very coarse at 9 Gyr and above, and so caution against overinterpreting the age results in that region. We also find our galaxies to have slightly positive [α/Fe] gradients overall, though we caution that our grid sampling in terms of [α/Fe] is likewise coarse.

We present profiles of M_*/L_V in Fig. 24. We find three broad behaviours in the M_*/L_V profiles: we find a positive gradient for NGC 3626, a near-flat gradient for NGC 5631 and negative gradients for the remainder of the sample. This is interesting to consider

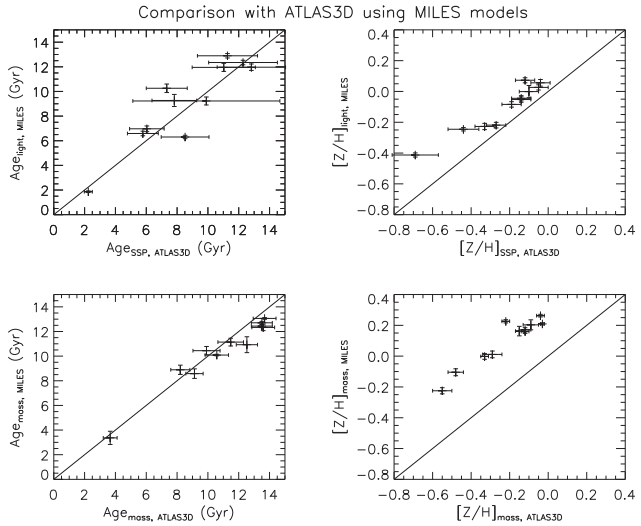

Figure 21. Comparison between stellar population parameters calculated around $1R_e$ apertures with those reported in McDermid et al. (2015) from ATLAS^{3D} data. The black solid lines indicate one-to-one relations. We find good agreement in terms of age and light-weighted [Fe/H], but find significant offsets in terms of mass-weighted [Fe/H].

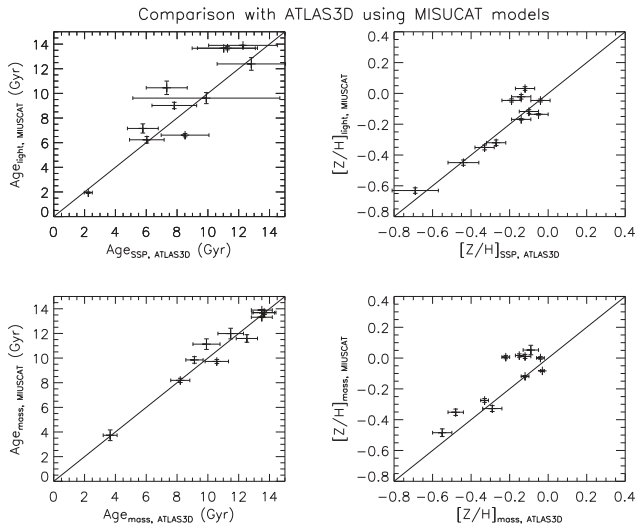

Figure 22. Comparison between stellar population parameters calculated around $1R_e$ apertures with MIUSCAT models with those reported in McDermid et al. (2015) from ATLAS^{3D} data. The black solid lines indicate one-to-one relations. We find good agreement in terms of age and light-weighted [Z/H], but continue to observe a mild offset in mass-weighted [Z/H].

in the context of ETG dynamics, given that M_*/L is typically assumed to be constant in dynamical modelling studies; we explore this point further in Section 6. Tortora et al. (2011) have previously investigated M_*/L variations by modelling SDSS imaging data out to $1R_e$ and report age gradients within galaxies to be the key factor in M_*/L behaviour. We tested for a similar relationship here. We first calculated global parameter gradients for each galaxy by performing least-absolute-deviation fits to our profiles, in log space. We then compared the gradients in light-weighted age, metallicity and abundance ratio with the gradients derived for M_*/L_V; we show the results of this in Fig. 25, in which we also show the linear Pearson correlation coefficient R in each instance. We find a strong

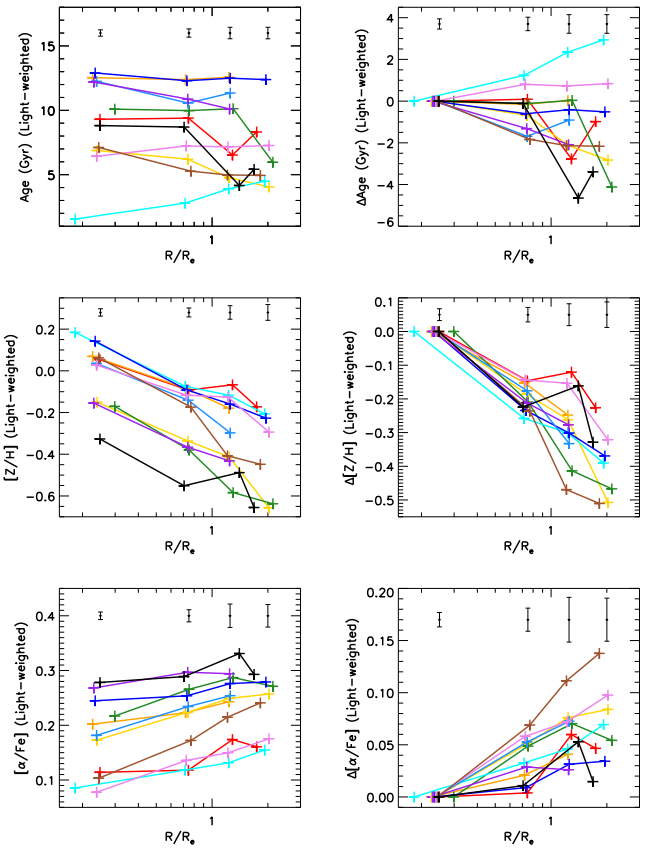

Figure 23. Absolute (left) and relative (right) profiles of light-weighted age (top), metallicity (middle) and [α/Fe] abundance ratio, derived from PPXF fits to combined spectra. Lines are as in Fig. 14. The black error bars show the mean error at a given aperture or annulus position.

correlation between the gradients for M_*/L_V and age, with only weak correlations between the gradients in M_*/L_V and those for metallicity or abundance ratio; as such, the changes in age appear to be the main cause of the M_*/L_V gradients. We find median gradients of -0.047 dex/dex, -0.38 dex/dex and 0.056 dex/dex for galaxies' light-weighted age, metallicity and abundance ratio, respectively. We also find a median M_*/L_V gradient of -0.16 dex/dex.

In Fig. 26, we plot the difference in light-weighted and mass-weighted values obtained for the galaxies' stellar age profiles. Most of our galaxies show mild differences of approximately 1 Gyr, with little evolution with radius; this is indicative of the galaxies containing single dominant stellar populations. NGC 6798 is an exception here, showing large differences at low radii. NGC 3626 notably does *not* show differences significantly higher than the remainder of the sample, despite appearing significantly younger than NGC 6798 in a light-weighted sense.

In Fig. 27, we present the SSP mass-weight maps from the regularized SSP PPXF fits to NGC 3626 in terms of age and metallicity. We find the fits to predict a significant young stellar population component in the centre of NGC 3626, which becomes increasingly sub-dominant at larger radii. Near the centre of NGC 3626, the young stellar populations are significant in both a mass-weighted and light-weighted sense. Further out, such populations contribute little to the mass but continue to contribute to light-weighted parameters due to the relative brightness of young stars; which explains the behaviour for this galaxy seen in Fig. 26, in which the

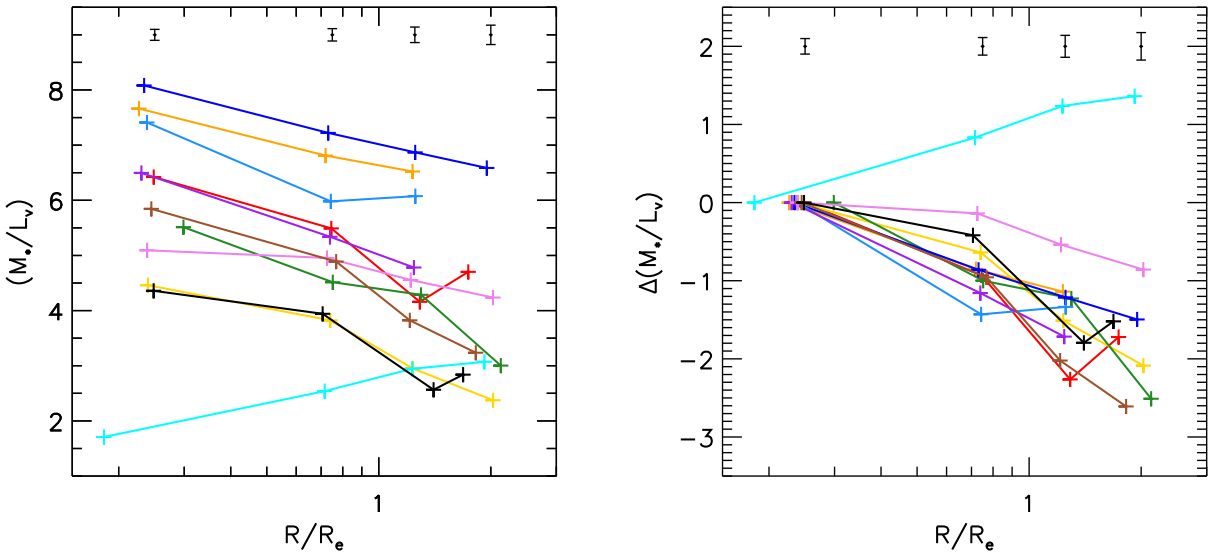

Figure 24. Absolute (left) and relative (right) profiles of stellar mass-to-light ratio M_*/L_V, derived from PPXF fits to combined spectra. Lines are as in Fig. 14, with error bars showing the mean error at a given aperture or annulus.

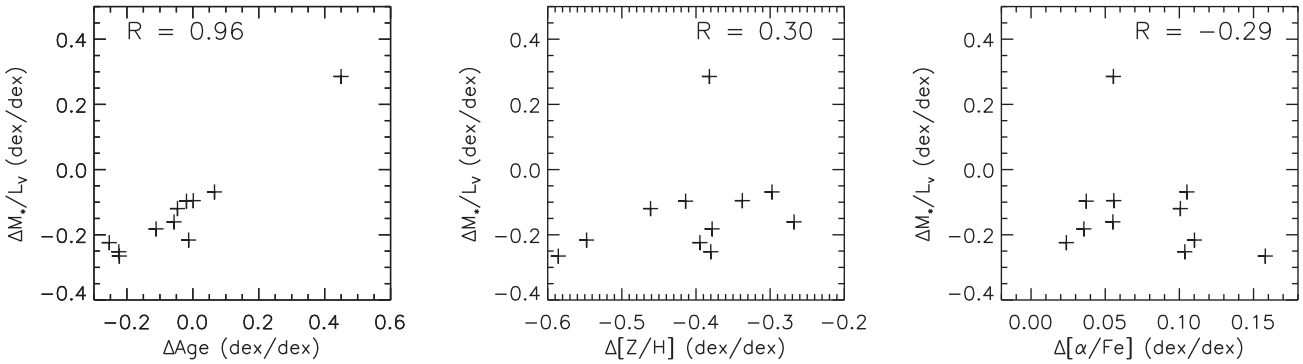

Figure 25. Gradients in M_*/L_V plotted as a function of age, metallicity and abundance ratio. Individual parameters are as discussed in the text. The M_*/L_V gradient correlates strongly with age while showing little dependence on metallicity or abundance ratio, implying that age variations are the main driver of the M_*/L_V gradients in our results.

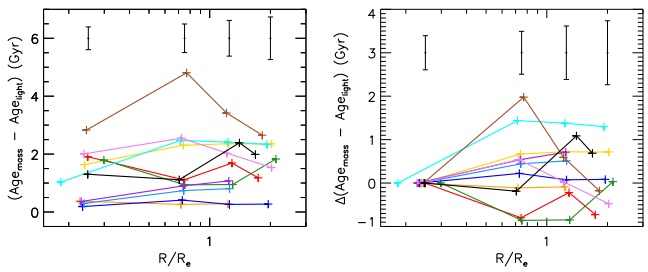

Figure 26. Profiles of the difference between light-weighted and mass-weighted galaxy ages. Line colours are same as in Fig. 14. We find mild differences of approximately 1–2 Gyr in most cases, but we find a larger difference for NGC 6798 (brown line).

difference between light-weighted and mass-weighted age increases with radius.

We present NGC 6798's mass-weight maps in Fig. 28, in which we find NGC 6798 to be dominated by an old population throughout the tested FOV. A young sub-population is also present, however, which is emphasized by the spike in this galaxy's profile seen in Fig. 26; this sub-population becomes significantly more apparent when flux weighting is considered, as shown in Fig. 29.

6 DISCUSSION

In the previous sections, we presented stellar kinematics for our sample of ETGs. We probed for any stellar kinematics transitions beyond $1R_e$, using the λ_R parameter as a proxy for angular momentum. We extracted ionized gas fluxes and kinematics and showed a significant fraction of our galaxies to contain ionized gas that is misaligned with the galaxies' stars. Lastly, we performed spectral fitting with SSP models in order to investigate the galaxies' stellar populations.

Visually, we see no dramatic changes in the stellar kinematics beyond $1R_e$: galaxies with significant rotation at $1R_e$ remain fast rotating as far out as we observe, and slow-rotating galaxies likewise remain slow rotating. Our λ_R profiles support this view, with no dramatic changes seen beyond $1R_e$. Crucially, we observe no *decreases* of these parameters with position beyond the central half-light radius. We therefore confirm that the fast/slow-rotator classification (Emsellem et al. 2007) seems to generally characterize well the overall dynamical status of our sample galaxies' stellar

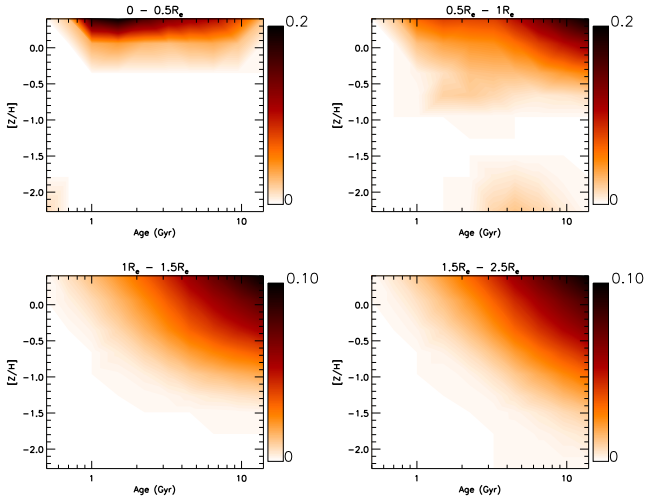

Figure 27. Mass-weight maps from PPXF SSP model fits to NGC 3626. At the centre, this galaxy contains both significant young and old populations (top left window); at larger radii, the fits are consistent with the galaxy being dominated by old stars.

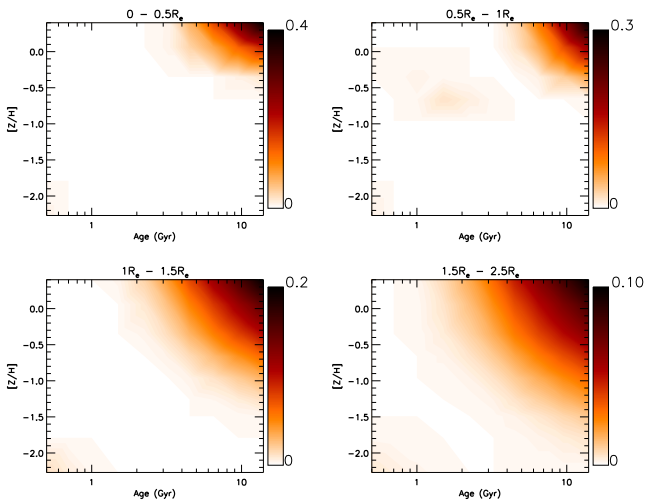

Figure 28. Mass-weight maps from PPXF SSP model fits to NGC 6798. We find this galaxy's mass to be dominated by old stars across the tested FOV, with signs also of younger sub-populations as seen in the right-hand windows.

populations. Our kinematic results are different to those of Arnold et al. (2014), who report declines in specific angular momentum beyond $1R_e$ in a few cases and who argue this to signify a transition to stellar halo dominated outskirts and so late dry accretion, but are qualitatively similar to the those of Raskutti et al. (2014).

The apparent contrast between our results and those of Arnold et al. (2014) is due to differences between our sample and theirs. Eight out of our nine FRs would be classified as lenticular galaxies on the basis of their Hubble T-type parameter (T-type > -3.5; Paturel et al. 2003); the majority of Arnold et al. (2014) FRs would be classified as ellipticals on this basis and include multiple discy ellipticals, or E(d)s. E(d)s are characterized by a stellar disc that only dominates the light within the central regions, leading to drops in observed stellar rotation beyond $\sim 1R_e$. Most FRs are instead dominated by rotation out to large radii, meaning that drops in momentum are not generally observed (e.g. Coccato et al. 2009). This difference in the kinematic behaviour of FRs at large radii

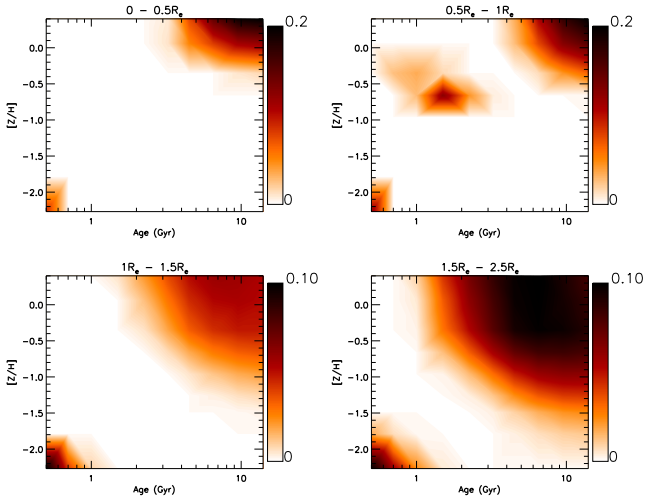

Figure 29. Flux-weight maps from PPXF SSP model fits to NGC 6798. A young sub-populations of stars is apparent in the fits.

is illustrated in fig. 3 of Cappellari (2016), and our observations appear consistent with this general picture.

Röttgers, Naab & Oser (2014) have found in their simulations that *in situ* and *ex situ* formed stars follow similar orbit distributions; as such, it is difficult to rule out late dry accretion from the kinematics alone. However, we note that the λ_R profiles for our FRs are very similar in shape to those presented in Naab et al. (2014), which are based on the same simulations as Röttgers et al. (2014), for galaxies that have experienced late ($z < 2$) gas-rich mergers and/or gradual dissipation. As such, we find our λ_R profiles to be consistent with gas-rich histories for these galaxies. We reiterate at this point that we selected our sample based on the presence of H I; as such, the similarity of our profiles to those of the gas-rich Naab et al. (2014) galaxies is unsurprising but is nonetheless encouraging.

The ionized gas content of these galaxies also supports the idea of several of them them having experienced gas-rich events in their pasts, with significant misalignments between the gaseous and stellar components in several cases. We find counter-rotating gas in NGC 3626, NGC 5631 and NGC 6798. The gas kinematics for both NGC 2685 and NGC 3998 show signs of warps, with NGC 3998's case in particular resembling the simulated gas disc in van de Voort et al. (2015), while NGC 3522 features a polar-rotating gas disc. Such features imply that the gas in these galaxies was accreted after the galaxies themselves were formed, or else was disturbed and then subsequently re-accreted. Such arguments could also hold for some corotating ionized gas structures, since an accreted gas disc should ultimately align with its host galaxy's stars in half of all cases (e.g. Katkov, Kniazev & Sil'chenko 2015); the time-scales of such alignments (or anti-alignments) will vary from object to object, but could potentially be several Gyr in the case of extended accretion (van de Voort et al. 2015).

Our stellar population modelling results also appear to discount late dry major mergers for the 11 galaxies that we modelled, as well as late major mergers in general. Here, we find that the metallicity continues to decline well beyond the central effective radius, with little change seen in metallicity gradients beyond $1R_e$. Gas-rich major mergers are predicted to steepen metallicity gradients within approximately $1R_e$ (Hopkins et al. 2009), which is not supported by our modelling. Gas-poor major mergers, meanwhile, are predicted to flatten metallicity gradients; Kobayashi (2004), for instance, find

a mean typical metallicity gradient of −0.19 dex/dex from their major merger simulations. Our stellar population modelling yields metallicity gradients that are typically steeper than predicted to result from dry major mergers, with our stellar kinematics likewise inconsistent with late dry major merging. Our results are therefore consistent with our galaxies having not experienced major mergers at late times.

Our metallicity gradients also agree well with those from the cosmological simulations of Hirschmann et al. (2015) in the case when galactic winds are included, which yield metallicity gradients of −0.35 dex/dex; their wind-free simulations, by contrast, yield a mean gradient of just −0.11 dex/dex. Hirschmann et al. (2015) find that galactic winds lower the rate of stellar accretion in their models while also lowering the metallicity of accreted stars, with stellar accretion then serving the steepen the metallicity gradient. As such, our results are not inconsistent with dry minor mergers and/or accretion events having occurred.

Our investigation of the Mg b–σ relation beyond $1R_e$ shows this relation to persist beyond the central effective radius, meanwhile, with similar Mg b gradients for most of our galaxies leading to correspondingly similar gradients in the Mg b–σ relation out to large radii. We infer from this that the galaxies in our sample have had broadly similar evolution histories, which we ascribe in turn to our selection criteria.

We found positive [α/Fe] gradients for all galaxies for which we performed stellar population modelling. [α/Fe] has previously been shown to be linked to the formation time-scale of stellar populations, with populations with greater α-enhancement having shorter time-scales on average (e.g. Thomas et al. 2005; McDermid et al. 2015). As such, our results here indicate that the stars in our ETGs have shorter formation time-scales at larger radii. This result is similar to those that have previously been reported in bulges of galaxies across the Hubble sequence (Jablonka, Gorgas & Goudfrooij 2007), as well as to the vertical gradients reported for barred disc galaxies (Molaeinezhad et al. 2017).

We found negative age gradients in most cases, with a strong positive age gradient for NGC 3626. NGC 3626 is relatively young compared to most ETGs, being younger than 5 Gyr throughout the tested FOV in a light-weighted sense. We also compared the light-weighted stellar ages of our galaxies with the mass-weighted values, finding a significant difference in the case of NGC 6798. We demonstrated this to be due to young bright sub-populations of stars, which contribute much to a galaxy's luminosity but only a little to its overall mass budget. Such findings could indicate that galaxies such as NGC 3626 and NGC 6798 are undergoing quenching for the first time, or else could indicate that they are experiencing a degree of rejuvenation. Given the presence of misaligned ionized gas in several of our galaxies, we argue that the latter interpretation is more likely: these galaxies experience gas-rich interaction events that subsequently triggered some amount of star formation. Even a small amount of star formation will significantly decrease the SSP light-weighted age result due to the brightness of young stars (e.g. Scott et al. 2013); as these galaxies age, this bright young population will fade, causing their age profiles to more closely resemble the older ETGs in our sample.

Deep imaging has also yielded signs of past interactions for several of the galaxies in our sample. Duc et al. (2015) report finding signs of recent wet merging in NGC 2685 and NGC 2764; they further report tidal disturbances in NGC 680, a possible disrupted satellite 50 kpc north of NGC 3522, and multiple internal shells within NGC 5631. As such, we find our results to be consistent with the implications of the Duc et al. (2015) imaging.

Of the 10 galaxies classified as 'D' in Serra et al. (2012), 9 show signs of some past disturbance in their H I morphologies. Both NGC 3626 and NGC 6798 contain counter-rotating H I discs, while other H I structures within our 'D' galaxies display warps, lopsidedness and/or kinematic misalignments with respect to galaxies' stellar kinematics. NGC 5582 is the one exception here, with its H I content consisting of a large-scale ring that is well aligned with the stellar content. The large-scale H I content of these 10 galaxies appears to rule out significant late-time major merging, since this would disrupt the H I disc structure, but also appears to signify the need for interaction events in nearly all of these galaxies' pasts; this agrees well with the picture we have derived from our IFU data, as well as that which can be implied from deep optical imaging.

Both NGC 680 and NGC 1023 are classified as 'u' in Serra et al. (2012), indicating substantially unsettled H I morphology; it is therefore harder to constrain the pasts of these two systems on the basis of H I alone. However, these galaxies do not display significantly different behaviour from the rest of the sample in terms of their λ_R profiles or stellar populations, and so we argue that these galaxies most likely experienced one or more gas-rich interaction events in a similar manner to the rest of our sample.

Lastly, we found our SSP models to support negative M_*/L_V gradients for the majority of our sample. Such gradients could have important implications for dynamical modelling of ETGs. Dynamical models of ETGs generally assume a flat M_*/L slope. Attempts to calculate M_*/L slopes in dynamical models are few and far between, but typically produce positive M_*/L gradients due to the degeneracy between dark and visible mass (e.g. Yıldırım et al. 2016). Our results imply that dynamical models of many of our ETGs would have biases in the inferred dark matter contributions were M_*/L to be assumed fixed. Given that ETGs have generally been found to contain only low amounts of dark matter within their central half-light radius (e.g. Boardman et al. 2016; Cappellari et al. 2013a), our results demonstrate the need for allowing for M^*/L gradients in dynamical models, as done for instance in Mitzkus, Cappellari & Walcher (2017) and Poci, Cappellari & McDermid (2017).

An important caveat is that we did not attempt to account for dust attenuation in our SSP fits; this is because the effects of attenuation are degenerate with the continuum correction over our wavelength range. Undetected dust gradients could therefore play a role in our detected stellar population gradients and, in turn, our M_*/L_V gradients. It would be illuminating to perform a similar stellar population analysis for IFU spectra with wider wavelength ranges, for which the effects of dust could be accounted for in a non-degenerate way.

7 SUMMARY AND CONCLUSION

We have presented an IFU sample of 12 nearby H I-detected ETGs of intermediate mass, for which we obtain stellar and gaseous kinematics. We also obtain stellar population constraints out to multiple effective radii for 11 out of the 12 galaxies. Our study represents the first IFU analysis of such objects far beyond the central effective radius, allowing for valuable comparisons to simulations that could not previously have been made. Our ETGs have also been observed previously as part of the ATLAS^{3D} survey, making our data greatly complimentary to high-spatial resolution central IFU data provided by that survey.

We find no large transitions in the stellar kinematics beyond $1R_e$: galaxies in our sample that are FRs (SRs) at $1R_e$ retain a high (low) λ_R amplitude over the full FOV of our data relative to their respective ellipticities. We find encouraging agreement between the observed fast-rotator kinematics and those from simulations, with

the spin profiles of our FRs strongly resembling those of simulated galaxies with gas-rich histories.

Our results in terms of stellar metallicity, meanwhile, appear to rule out late major merging for our galaxies. We find metallicity gradients that persist to multiple half-light radii for the 11 galaxies we modelled, with no clear flattening beyond $1R_e$. Were these galaxies to have experienced gas-rich major mergers at late times, then we would not expect such trends to survive. Our derived metallicity gradients are typically steeper than would be expected for remnants of dry major mergers, meanwhile. Our results here therefore demonstrate complimentary nature of stellar kinematics and stellar populations for uncovering ETG's histories.

We show that a significant fraction of our galaxies contained ionized gas that is counter rotating or else misaligned with respect to the stars; this is not a new result for these galaxies, but highlights the fact that many of these galaxies cannot have had completely passive histories. Our stellar population modelling further suggest past interactions in certain cases, with noticeable age gradients in certain ETGs as well as multiple stellar population components arising from modelling of certain objects. As such, both our ionized gas measurements and stellar population modelling produce results consistent with those obtained for the galaxies' stellar kinematics.

We also find our stellar population modelling to imply negative gradients in M_*/L_V for the majority of galaxies in our sample. This could have important implications for dynamical models of ETGs, for which the mass-to-light ratio is typically assumed constant and for which the central dark matter fractions are typically found to be low. We thus argued that it could be worthwhile to consider this in future dynamical modelling works.

In this paper, we have demonstrated both the reach of our observations and their power in investigating ETG's histories. We have shown that all approaches of analysing our spectra paint a consistent evolutionary picture: the galaxies in our sample were likely shaped by at least one gas-rich interaction apiece, with late dry major mergers ruled out by the data. We have thus shown that a wide FOV is crucial for investigating the formation paths of ETGs, with much information to be found beyond the central half-light radius.

ACKNOWLEDGEMENTS

We wish to thank Josh Adams, Guillermo Blanc and Jeremy Murphy for their help with the data reduction. We thank Vivienne Wild and Marc Sarzi for fruitful discussions concerning our analysis. We thank Adam Atkinson, Phil Cigan, Carina Lagerholm, Kevin Luecke and Kristina Nyland for their help with observing, and we thank the staff of McDonald Observatory for their support. We thank Anne Sansom for her useful and thorough referee report, which significantly improved this paper. NFB was supported by STFC grant ST/K502339/1 during the course of this work. NFB acknowledges support from the Max Planck Institute for Astronomy in Heidelberg, Germany. AW acknowledges support of a Leverhulme Trust Early Career Fellowship. MC acknowledges support from a Royal Society University Research Fellowship. JF-B acknowledges support from grant AYA2016-77237-C3-1-P from the Spanish Ministry of Economy and Competitiveness (MINECO).

REFERENCES

Adams J. J. et al., 2011, ApJS, 192, 5
Ahn C. P. et al., 2014, ApJS, 211, 17
Arnold J. A. et al., 2014, ApJ, 791, 80
Bacon R. et al., 2001, MNRAS, 326, 23
Blanc G. A. et al., 2013, AJ, 145, 138
Boardman N. F. et al., 2016, MNRAS, 460, 3029
Brodie J. P. et al., 2014, ApJ, 796, 52
Cappellari M., 2013, ApJ, 778, L2
Cappellari M., 2016, ARA&A, 54, 597
Cappellari M., 2017, MNRAS, 466, 798
Cappellari M., Copin Y., 2003, MNRAS, 342, 345
Cappellari M., Emsellem E., 2004, PASP, 116, 138
Cappellari M. et al., 2006, MNRAS, 366, 1126
Cappellari M. et al., 2011a, MNRAS, 413, 813
Cappellari M. et al., 2011b, MNRAS, 416, 1680
Cappellari M. et al., 2013a, MNRAS, 432, 1862
Cappellari M. et al., 2013b, MNRAS, 432, 1709
Cimatti A., Nipoti C., Cassata P., 2012, MNRAS, 422, L62
Coccato L. et al., 2009, MNRAS, 394, 1249
Coccato L., Gerhard O., Arnaboldi M., 2010, MNRAS, 407, L26
Davies R. L., Sadler E. M., Peletier R. F., 1993, MNRAS, 262, 650
Davis T. A. et al., 2011, MNRAS, 417, 882
de Zeeuw P. T. et al., 2002, MNRAS, 329, 513
Dressler A. et al., 1997, ApJ, 490, 577
Duc P.-A. et al., 2015, MNRAS, 446, 120
Emsellem E. et al., 2007, MNRAS, 379, 401
Emsellem E. et al., 2011, MNRAS, 414, 888
Fabian A. C., 2012, ARA&A, 50, 455
Falcón-Barroso J., Sánchez-Blázquez P., Vazdekis A., Ricciardelli E., Cardiel N., Cenarro A. J., Gorgas J., Peletier R. F., 2011, A&A, 532, A95
Falcón-Barroso J., Lyubenova M., van de Ven G., 2015, in Cappellari M., Courteau S., eds, Proc. IAU Symp. 311, Galaxy Masses as Constraints of Formation Models. Cambridge Univ. Press, Cambridge. p. 78
Graves G. J., Faber S. M., Schiavon R. P., 2009, ApJ, 698, 1590
Greene J. E., Murphy J. D., Graves G. J., Gunn J. E., Raskutti S., Comerford J. M., Gebhardt K., 2013, ApJ, 776, 64
Greene J. E., Janish R., Ma C.-P., McConnell N. J., Blakeslee J. P., Thomas J., Murphy J. D., 2015, ApJ, 807, 11
Hill G. J. et al., 2008, Proc. SPIE, 7014, 701470
Hirschmann M., Naab T., Ostriker J. P., Forbes D. A., Duc P.-A., Davé R., Oser L., Karabal E., 2015, MNRAS, 449, 528
Hopkins P. F., Cox T. J., Dutta S. N., Hernquist L., Kormendy J., Lauer T. R., 2009, ApJS, 181, 135
Jablonka P., Gorgas J., Goudfrooij P., 2007, A&A, 474, 763
Katkov I. Y., Kniazev A. Y., Sil'chenko O. K., 2015, AJ, 150, 24
Kelson D. D., 2003, PASP, 115, 688
Khochfar S., Silk J., 2006, ApJ, 648, L21
Kobayashi C., 2004, MNRAS, 347, 740
Krajnović D., Cappellari M., de Zeeuw P. T., Copin Y., 2006, MNRAS, 366, 787
Krajnović D. et al., 2011, MNRAS, 414, 2923
Ma C.-P., Greene J. E., McConnell N., Janish R., Blakeslee J. P., Thomas J., Murphy J. D., 2014, ApJ, 795, 158
Martín-Navarro I., Brodie J. P., van den Bosch R. C. E., Romanowsky A. J., Forbes D. A., 2016, ApJ, 832, L11
McDermid R. M. et al., 2015, MNRAS, 448, 3484
Mitzkus M., Cappellari M., Walcher C. J., 2017, MNRAS, 464, 4789
Molaeinezhad A., Falcón-Barroso J., Martínez-Valpuesta I., Khosroshahi H. G., Vazdekis A., La Barbera F., Peletier R. F., Balcells M., 2017, MNRAS, 467, 353
Naab T. et al., 2014, MNRAS, 444, 3357
Oser L., Ostriker J. P., Naab T., Johansson P. H., Burkert A., 2010, ApJ, 725, 2312
Oser L., Naab T., Ostriker J. P., Johansson P. H., 2012, ApJ, 744, 63
Pastorello N., Forbes D. A., Foster C., Brodie J. P., Usher C., Romanowsky A. J., Strader J., Arnold J. A., 2014, MNRAS, 442, 1003
Paturel G., Petit C., Prugniel P., Theureau G., Rousseau J., Brouty M., Dubois P., Cambrésy L., 2003, A&A, 412, 45
Peng Y., Maiolino R., Cochrane R., 2015, Nature, 521, 192
Poci A., Cappellari M., McDermid R. M., 2017, MNRAS, 467, 1397
Prugniel P., Soubiran C., 2001, A&A, 369, 1048

Querejeta M. et al., 2015, A&A, 579, L2
Raskutti S., Greene J. E., Murphy J. D., 2014, ApJ, 786, 23
Rawle T. D., Smith R. J., Lucey J. R., Swinbank A. M., 2008, MNRAS, 389, 1891
Röttgers B., Naab T., Oser L., 2014, MNRAS, 445, 1065
Sánchez-Blázquez P. et al., 2006, MNRAS, 371, 703
Sarzi M. et al., 2006, MNRAS, 366, 1151
Schiavon R. P., 2007, ApJS, 171, 146
Scott N. et al., 2013, MNRAS, 432, 1894
Serra P. et al., 2012, MNRAS, 422, 1835
Serra P. et al., 2014, MNRAS, 444, 3388
Thomas D., Maraston C., Bender R., Mendes de Oliveira C., 2005, ApJ, 621, 673
Tortora C., Napolitano N. R., Romanowsky A. J., Jetzer P., Cardone V. F., Capaccioli M., 2011, MNRAS, 418, 1557
Trujillo I. et al., 2006, ApJ, 650, 18
Vaghmare K., Barway S., Mathur S., Kembhavi A. K., 2015, MNRAS, 450, 873
van de Voort F., Davis T. A., Kereš D., Quataert E., Faucher-Giguère C.-A., Hopkins P. F., 2015, MNRAS, 451, 3269
van Dokkum P. G. et al., 2010, ApJ, 709, 1018
van Dokkum P. G. et al., 2013, ApJ, 771, L35
Vazdekis A., Sánchez-Blázquez P., Falcón-Barroso J., Cenarro A. J., Beasley M. A., Cardiel N., Gorgas J., Peletier R. F., 2010, MNRAS, 404, 1639
Vazdekis A., Ricciardelli E., Cenarro A. J., Rivero-González J. G., Díaz-García L. A., Falcón-Barroso J., 2012, MNRAS, 424, 157
Vazdekis A. et al., 2015, MNRAS, 449, 1177
Weijmans A.-M. et al., 2009, MNRAS, 398, 561
Wilkinson D. M. et al., 2015, MNRAS, 449, 328
Worthey G., Faber S. M., Gonzalez J. J., Burstein D., 1994, ApJS, 94, 687
Wu X., Gerhard O., Naab T., Oser L., Martinez-Valpuesta I., Hilz M., Churazov E., Lyskova N., 2014, MNRAS, 438, 2701
Yıldırım A. et al., 2016, MNRAS, 456, 538

SUPPORTING INFORMATION

Supplementary data are available at *MNRAS* online.

Figure S1. Maps of indices H β, Fe5015, Mg b, Fe5270 and Fe5335 for NGC 680, NGC 1023 and NGC 2685.
Figure S2. Same as in Fig. S1, but for galaxies NGC 2764, NGC 3522 and NGC 3626.
Figure S3. Same as in Fig. S1, but for galaxies NGC 3998, NGC 4203 and NGC 5582.
Figure S4. Same as in Fig. S1, but for galaxies NGC 5631, NGC 6798 and UGC 03960.

Please note: Oxford University Press is not responsible for the content or functionality of any supporting materials supplied by the authors. Any queries (other than missing material) should be directed to the corresponding author for the article.

This paper has been typeset from a TEX/LATEX file prepared by the author.